NASA/TM–2013-217977

Experimental Investigation of Aeroelastic Deformation of Slender Wings at Supersonic Speeds Using a Video Model Deformation Measurement Technique

Gary E. Erickson
Langley Research Center, Hampton, Virginia

April 2013

NASA STI Program . . . in Profile

Since its founding, NASA has been dedicated to the advancement of aeronautics and space science. The NASA scientific and technical information (STI) program plays a key part in helping NASA maintain this important role.

The NASA STI program operates under the auspices of the Agency Chief Information Officer. It collects, organizes, provides for archiving, and disseminates NASA's STI. The NASA STI program provides access to the NASA Aeronautics and Space Database and its public interface, the NASA Technical Report Server, thus providing one of the largest collections of aeronautical and space science STI in the world. Results are published in both non-NASA channels and by NASA in the NASA STI Report Series, which includes the following report types:

- TECHNICAL PUBLICATION. Reports of completed research or a major significant phase of research that present the results of NASA Programs and include extensive data or theoretical analysis. Includes compilations of significant scientific and technical data and information deemed to be of continuing reference value. NASA counterpart of peer-reviewed formal professional papers, but having less stringent limitations on manuscript length and extent of graphic presentations.

- TECHNICAL MEMORANDUM. Scientific and technical findings that are preliminary or of specialized interest, e.g., quick release reports, working papers, and bibliographies that contain minimal annotation. Does not contain extensive analysis.

- CONTRACTOR REPORT. Scientific and technical findings by NASA-sponsored contractors and grantees.

- CONFERENCE PUBLICATION. Collected papers from scientific and technical conferences, symposia, seminars, or other meetings sponsored or co-sponsored by NASA.

- SPECIAL PUBLICATION. Scientific, technical, or historical information from NASA programs, projects, and missions, often concerned with subjects having substantial public interest.

- TECHNICAL TRANSLATION. English-language translations of foreign scientific and technical material pertinent to NASA's mission.

Specialized services also include organizing and publishing research results, distributing specialized research announcements and feeds, providing information desk and personal search support, and enabling data exchange services.

For more information about the NASA STI program, see the following:

- Access the NASA STI program home page at *http://www.sti.nasa.gov*

- E-mail your question to help@sti.nasa.gov

- Fax your question to the NASA STI Information Desk at 443-757-5803

- Phone the NASA STI Information Desk at 443-757-5802

- Write to:
  STI Information Desk
  NASA Center for AeroSpace Information
  7115 Standard Drive
  Hanover, MD 21076-1320

NASA/TM–2013-217977

Experimental Investigation of Aeroelastic Deformation of Slender Wings at Supersonic Speeds Using a Video Model Deformation Measurement Technique

Gary E. Erickson
Langley Research Center, Hampton, Virginia

National Aeronautics and
Space Administration

Langley Research Center
Hampton, Virginia 23681-2199

April 2013

Acknowledgments

The following individuals at NASA Langley Research Center are acknowledged for their helpful discussions and contributions to this paper: Alpheus W. Burner, Kenneth H. Cate, Harriet R. Dismond, John R. Micol, Floyd J. Wilcox, and Ricky L. Hall.

Available from:

NASA Center for AeroSpace Information
7115 Standard Drive
Hanover, MD 21076-1320
443-757-5802

Table of Contents

Table of Contents v
Abstract 1
Introduction 1
Nomenclature 2
Wind Tunnel Facility 2
Wind Tunnel Models 3
Wind Tunnel Test Conditions 4
VMD System Description, Calibration, and Wind-On Image Processing 4
  VMD System Components 4
  VMD System Calibration 5
  Wind-On Image Acquisition and Processing 6
Discussion of Results 7
  Flapped Wing 7
    Span Station Sweeps 7
    Mach Number Sweeps 7
    Reynolds Number/Dynamic Pressure Sweeps 7
    Data Repeatability 8
  Solid Wing 8
    Span Station Sweeps 8
    Mach Number Sweeps 8
  Comparison of Flapped and Solid Wings 8
Summary 9
References 9
Table 10
Figures 11

This page intentionally left blank.

Abstract

A video-based photogrammetric model deformation system was established as a dedicated optical measurement technique at supersonic speeds in the NASA Langley Research Center Unitary Plan Wind Tunnel. This system was used to measure the wing twist due to aerodynamic loads of two supersonic commercial transport airplane models with identical outer mold lines but different aeroelastic properties. One model featured wings with deflectable leading- and trailing-edge flaps and internal channels to accommodate static pressure tube instrumentation. The wings of the second model were of single-piece construction without flaps or internal channels. The testing was performed at Mach numbers from 1.6 to 2.7, unit Reynolds numbers of 1.0 x 10^6 to 5.0 x 10^6, and angles of attack from -4 degrees to +10 degrees. The video model deformation system quantified the wing aeroelastic response to changes in the Mach number, Reynolds number concurrent with dynamic pressure, and angle of attack and effectively captured the differences in the wing twist characteristics between the two test articles.

Introduction

Model deformation may be defined as the change in shape of a model, particularly the wings and control surfaces, under aerodynamic load in a wind tunnel (references 1-6). The aerodynamic characteristics obtained in wind tunnel testing of a flexible model may differ from expected results or from computational fluid dynamics (CFD) predictions based on rigid body assumptions. Reference 7 compares three optical techniques that have been assessed at the National Aeronautics and Space Administration's Langley Research Center (NASA LaRC) for measuring model deformation, which include video photogrammetry, projection moiré interferometry (PMI), and the commercially-available Optotrak™ system. The fundamental technique used at the NASA LaRC Unitary Plan Wind Tunnel (UPWT) to measure model deformation is photogrammetry, and the evolution of a video-based photogrammetry technique at NASA LaRC is summarized in reference 8. The primary application of the video model deformation (VMD) system at UPWT is wing twist measurements on supersonic transport airplane configurations. The basic hardware of the VMD system at UPWT is a charge-coupled device (CCD) camera, computer with frame grabber, diffuse light source, and array of retroreflective tape targets on the model. The VMD technique consists of a single-camera, single-view, photogrammetric solution from digital images of targets placed on the wing at known semi-span locations. A photograph of a supersonic transport airplane model with wing targets installed for model deformation testing in UPWT is shown in figure 1. The videogrammetric system determines the spatial coordinates of the targets from the target centroids in the images, and then computes the model twist and bending (deflection) produced by the aerodynamic loads. The initial application of a VMD system at UPWT was in 1996 as part of a unified optical measurement technique development program at NASA (reference 9). An outcome of this work was the implementation of a dedicated UPWT VMD system described herein. The current report provides an overview of the UPWT VMD hardware, setup, calibration, and operational procedures and representative results from a specific application to two supersonic commercial transport airplane models with identical outer mold lines but different aeroelastic properties.

Nomenclature

b	local wing span, inches (in.)
b_{ref}	reference wing span, 26.383 in.
B. L.	butt line, in.
c_{ref}	reference length, 19.085 in.
CAD	computer-aided design
CCD	charge coupled device
CFD	computational fluid dynamics
DESL	data engineering scripting language
H_o	stagnation pressure, psfa
Mach	free stream Mach number
M_∞	free stream Mach number
Mode	tunnel operating mode
M. S.	model station, in.
OML	outer mold line
psfa	pounds per square foot absolute
psia	pounds per square inch absolute
PC	personal computer
PMI	projection moiré interferometry
PSP	pressure sensitive paint
q	free stream dynamic pressure, psfa
Re/ft	unit Reynolds number
S_{ref}	reference area, 2.385 square feet (sq. ft.)
T_0	stagnation temperature, degrees Fahrenheit (^{o}F)
T. S.	test section
UPWT	Unitary Plan Wind Tunnel
VMD	video model deformation
X	retrotarget chordwise location in wind tunnel coordinate system, positive in free stream direction, in.
y	distance along wing local semi-span measured from wing centerline, in.
Y	retrotarget spanwise location in wind tunnel coordinate system, positive in direction of right wing tip, in.
Z	retrotarget vertical location in wind tunnel coordinate system, positive up, in.
α	angle of attack, deg
η	nondimensional semi-span location
θ	wing twist angle, degrees (negative leading edge down)
Δ	denotes delta value; in data repeatability analysis, Δ's are obtained by interpolating in each run to the nominal values of the independent variable, then averaging and subtracting the averages from the interpolated data

Wind Tunnel Facility

UPWT is a closed-circuit pressure tunnel with two test sections that are nominally 4 feet by 4 feet in cross section and 7 feet long. Detailed descriptions of UPWT are provided in reference 10 and reference 11. An aerial view of the facility is shown in figure 2. The primary elements of UPWT are a 100,000-horsepower compressor drive system, a dry air supply and evacuating system, a cooling system, and the necessary interconnecting ducting to produce the proper air flow through either of the two test sections. The Mach number range is approximately 1.47 to 2.86 in Test Section 1 and 2.30 to 4.63 in Test Section 2. The stagnation pressure can be varied up to a maximum of approximately 50 psia in Test Section 1 and approximately 100 psia in Test Section 2. The nozzle throat-to-test section area ratio is varied by a lower asymmetric sliding nozzle block that provides continuous variation of the Mach number. A cross-sectional illustration of the nozzle block is presented in figure 3. The second-minimum area is controlled by moving hinged sidewalls to provide the proper constriction to stabilize the normal shock downstream of the test section at the various operating Mach numbers. In order to cover the entire Mach number range for each test section, the tunnel duct configurations must be altered to provide the proper compression ratio. Six centrifugal compressors are used in five tunnel configurations or modes, and the tunnel operating modes are available for only one test section at a time. Test Section 1 has two modes within which the Mach number is varied from 1.47 to 2.16 in Mode 1-IA and 2.36 to 2.86 in Mode 1-II, respectively. Three modes exist in Test Section 2 within which the Mach number is varied from 2.30 to 2.96 in Mode 2-II, 3.00 to 3.71 in Mode 2-III, and 3.82 to 4.63 in

Mode 2-IV, respectively. The tunnel stagnation temperatures are typically 125° F and 150° F, depending on the mode of operation. Typical unit Reynolds numbers, Re/ft, for testing at UPWT are 2.0×10^6 to 4.0×10^6, although a range of unit Reynolds numbers from 1.0×10^6 to 5.0×10^6 can be easily accommodated. A unit Reynolds number of 6.0×10^6 is possible on a selected basis only because of tunnel drive system operational limits.

Several methods to support the model have been used, but the basic mechanism is a horizontal wall-mounted strut which is capable of forward and aft travel of over 3 feet in the streamwise direction. A main sting support is attached to the strut and has lateral traverse and sideslip motion of +/-20 inches and +/-12 degrees, respectively. Forward of the main sting support is the angle-of-attack mechanism which provides pitch motion from -15 degrees to +30 degrees. A roll mechanism can be installed ahead of the pitch mechanism to provide continuous roll motion with a range of 360 degrees. The model is mounted to the roll mechanism or the pitch mechanism by means of a wide assortment of available stings. Figure 4 illustrates the overall test section layout with the major support system components. Upgrades to the facility include a Tunnel Flow Control System for automated control of the tunnel stagnation pressure, stagnation temperature, and dewpoint and Model Attitude Control Systems for Test Sections 1 and 2 providing automated test sequencing for pitch, yaw, and roll angles, axial and lateral positions, and data acquisition.

Wind Tunnel Models

Two precision metal models of supersonic transport airplane configurations were used during this test. The models featured identical outer mold lines (OMLs) and had an overall length of 52.740 inches and wing span of 26.383 inches. A sketch of the model configuration is shown in figure 5. One model featured leading- and trailing-edge flap segments that could be deflected to prescribed angles using bolt-on brackets. This model was also instrumented with surface static pressure orifices on the wings and fuselage, which required machined channels within the wings to accommodate the stainless steel pressure tubing. A second model featured wings of single-piece construction with no flaps or pressure instrumentation. The two models are designated in this report at the "flapped wing" and "solid wing," respectively. Both models featured two flow-through engine nacelles (per side) mounted to the left and right wings. The flapped wing and solid wing models without engine nacelles are shown installed in UPWT Test Section 1 in figure 6 and figure 7, respectively. It is noted that the wings-vertical orientation of each model without engine nacelles is for illustrative purposes only. The models were tested in a wings-level position with nacelles on throughout the VMD investigation.

Each model was instrumented with an internal strain-gage balance for six-component force and moment measurements. Balance data were acquired during the VMD image acquisition but are not included in this report. The balance measurements were used, however, to correct the model attitude for balance and sting deflections caused by the aerodynamic loads and to estimate the flow angle corrections at each Mach number and Reynolds number. The balance was installed on a custom sting mounted to the UPWT main pitch support system in Test Section 1.

Five streamwise rows of adhesive retroreflective tape targets (retrotargets) for VMD measurements were installed on the right wing upper surface of each model as shown in figure 8 and figure 9. The targets are to be distinguished from several smaller fastener holes for the wing nacelles and flap brackets that are filled with dental plaster and boundary layer transition "trip dots" that also appear as white circles in the photographs. The retrotargets were approximately 0.004-in. thickness and had excellent adhesion to the metal model surface. Test results described in reference 8 indicated the targets were aerodynamically non-intrusive at supersonic speeds. The target row span

locations were previously shown in figure 5 and corresponded to 22.6%, 41.1%, 54.1%, 76.0%, and 99.1% of the local semi-span distance measured from the fuselage centerline, or $\eta = y/(b/2)$ values of 0.226, 0.411, 0.541, 0.760, and 0.991. These span locations were selected based on the wing trailing-edge flap breaks, which served as quantifiable and repeatable reference locations. Each of the first four target rows at $\eta = 0.226$, 0.411, 0.541, and 0.760 featured four retrotargets having 0.375-inch diameter with 1.00-inch spacing. The target row near the wing tip, or $\eta = 0.991$, featured three retrotargets having 0.25-inch diameter with 0.875-inch spacing.

Boundary layer transition trip dots with 0.010-inch height were applied to the wing leading edges, nacelle leading edges (inside and outside nacelle surfaces), and fuselage nose tip on both models. The trip dots were located 0.60 inches aft of the wing and nacelle leading edges measured in a streamwise direction and 1.00 inch from the nose measured along the model surface. The trip dot location, height, and size were based on extensive prior testing of similar models in UPWT as described in reference 12.

Wind Tunnel Test Conditions

All testing was performed in UPWT Test Section 1. The flapped wing model was tested at free-stream Mach numbers of 1.6, 1.8, 2.1, 2.4, and 2.7 at a unit Reynolds number of 4.0×10^6 or a Reynolds number of 6.36×10^6 based on the reference wing chord. The flapped model was also tested at unit Reynolds numbers of 1.0, 2.0, 3.0, and 5.0×10^6 (or 1.59, 3.18, 4.77, and 7.95×10^6 based on the reference wing chord) at $M_\infty = 2.1$. Test data were obtained on the solid wing model at free-stream Mach numbers of 1.6, 1.8, 2.1, 2.4, and 2.7 at a unit Reynolds number of 4.0×10^6 or a Reynolds number of 6.36×10^6 based on the reference wing chord. The stagnation temperature was maintained at 125 degrees Fahrenheit for all Mach numbers and Reynolds numbers. Table I summarizes the tunnel operating conditions during the VMD investigation.

Testing was conducted in both operating modes (Mode 1-IA and Model 1-II) in Test Section 1 in order to obtain Mach numbers from 1.6 to 2.7. This represented a significant time savings, since it eliminated full installations of both models in Test Section 2, where Mach numbers of 2.4 and 2.7 would typically be obtained (reference 10). The compromise to running at $M_\infty = 2.4$ and 2.7 in Mode 1-II in Test Section 1 was increased test section turbulence (reference 10). This did not affect the successful pursuit of the primary objective of this investigation, which was to demonstrate the utility of the UPWT VMD system as a viable model deformation measurement tool at supersonic speeds.

Angle of attack sweeps were conducted in pause mode in 0.5-degree increments from -4 degrees to +10 degrees. Angle of sideslip was 0 degrees throughout the testing. The model angle of attack was corrected for balance and sting deflections caused by the aerodynamic loads and for flow angularity in the test section for all Mach numbers and Reynolds numbers.

VMD System Description, Calibration, and Wind-On Image Processing

VMD System Components

In the UPWT VMD system, a video signal from a standard RS-170 solid state camera with 752 horizontal by 240 vertical pixels per field was routed to a frame grabber controlled by a personal computer (PC) workstation which recorded a predetermined number of video fields into the frame grabber memory. The adjustable field integration time of the CCD video camera was set to 1/250 second in order to reduce the effects of dynamics on image recording. A 10 to 100 millimeter (mm) focal length remote zoom lens was used for imaging. Both models were swept through a range of angle of attack at the outset of the installation in the wind tunnel, and adjustments were made to the focal length in order to bracket the targeted region on the right

wing through the desired range of angle of attack. Once the focal length providing the desired field of view was established, the lens remote control module was powered down to prevent inadvertent focal length changes. The illumination source was a fiber optic-based ring light mounted to the front of the camera lens. The intensity of this diffuse white light was adjustable and was tailored to the specific test setup and to each model. Figure 10 shows the primary components of the UPWT VMD system used in the current investigation.

The VMD system software described in reference 13 and reference 14 controlled the video capture hardware and automatically reduced and analyzed the sequence of raw images. Uncorrected values of the wing local angle of attack at all target rows were displayed real-time as each data point was acquired. The PC received selected test conditions from the wind tunnel host computer via an RS-232 communications link. In addition, image acquisition was coordinated with the wind tunnel data acquisition using a contact closure activation system.

Retrotargets were placed on the right wing upper surface at predetermined span locations and were uniformly distributed within a chordwise row. The target installations on the flapped and solid wing models in UPWT Test Section 1 were previously shown in figure 8 and figure 9, respectively. The chordwise and spanwise locations of the targets in the tunnel coordinate system were known from the reference locations on the flapped and solid wings. A template for target installation on both models was created from the wind tunnel model computer-aided design (CAD) drawing. The template installed on the model in the UPWT test section is shown in figure 11.

The camera and light source were positioned slightly above the model (resulting in an oblique view of the model) and clamped inside the webbing of the UPWT test section side wall adjacent to the targeted wing (figure 10). This provided excellent optical access to the model through the 1.5-inch thick optical-quality window. The proximity of the light source to the wing (about 1 to 2 feet depending on the target row) resulted in very high contrast images. Previous experience (reference 8) showed that automatic target location was faster and more reliable if the gray levels of the wing targets were significantly greater than the background. Glints from the highly-polished metal surface of the model were potential sources of error in the acquisition of the target centroids. As a result, regions of the wing that were susceptible to this undesired effect were identified on both models in the current investigation. A thin layer of flat black paint, aerodynamically non-intrusive at supersonic speeds (reference 8 and reference 15), was applied to eliminate the unwanted reflections. This caused the wing surface to appear dark after simple threshold removal, making it easier to automatically locate the retrotargets on the wing surface.

VMD System Calibration

Calibration of the VMD system yielded camera parameters consisting of the pointing angles, spatial location, and photogrammetric principal point (an effective camera focal length) in the tunnel coordinate system. A key element of the calibration process was the application of a photogrammetric resection method (references 1-6) applied to a target plate that was aligned to the coordinate system of the tunnel. The target plate was positioned just above the right wing surface at a precisely known spanwise position with respect to the fuselage centerline. The plate was painted flat black and featured a 7x7 array of retrotargets with known locations, as shown in figure 12. In addition to the target plate, the calibration setup featured lateral and vertical translation stages, dial gauges, and laboratory jacks. Figure 13 shows the calibration setup used in the current investigation. The target plate was translated to several known spanwise locations along an optical rail. The 49 targets or “blobs” in each image were digitized, and the centroids of the targets were estimated using a blob analysis

technique (references 1-6). Estimates of the blob centroid spatial locations were derived from photogrammetric resection. A commercially-available software package (reference 16) was used in conjunction with the VMD software (reference 13 and reference 14) to derive the camera parameters. The calibration was an iterative procedure featuring the determination of initial camera parameters followed by successive re-computations of the blob centroid files until the camera pointing angle, spatial location, and principal point values had converged. Additional measurements were made on the target plate for an in-situ check of the final calibration constants. The plate was translated to different vertical positions while maintaining a constant spanwise position, and the measured and known vertical positions were compared.

The calibration hardware was moved away from the model, and a final calibration step was conducted featuring the acquisition of model target images. An initial image was acquired with the model angle of attack set to 0 degrees. The VMD-computed mean angles of attack (or local slope angles in the vertical plane of symmetry) were recorded at each target row and inserted as zero-offset values to an input file that was read by the setup portion of the VMD software (reference 13 and reference 14). Image acquisition was repeated with the modified input file to confirm that the computed mean angles of attack at each target row were essentially zero. This process was analogous to the acquisition of balance wind-off zeroes (reference 8). A static pitch sweep of the targeted model was conducted next, and images were acquired over the same angle-of-attack range as the scheduled wind-on runs. This static sweep was similar to the required wind-on reference images for pressure-sensitive paint (PSP) testing (reference 8) and to a model weight tare run (reference 8), since the computed wind-off local angles of attack at each target row were applied as tares to the corresponding wind-on data. The static pitch sweep was repeated at the middle and end of the testing of each model as a check of the system stability. In addition, the entire in-situ VMD calibration process was performed for both the flapped and solid wing models to ensure the reproducibility of the camera parameters and the wind-off tares.

Wind-On Image Acquisition and Processing

VMD image acquisition and preliminary processing of the raw images were automated during the wind-on runs. Ninety video frames were acquired over a 1.5-second time period, and every third frame was used for image processing (30 frames total). The real-time display on the VMD PC workstation featured the uncorrected local slopes at each target row, and this information was updated as each data point was acquired. Final reduction and plotting of the model deformation results occurred off-line. The wind-off and wind-on image files created by the VMD software were processed using the computational software in reference 16. The local slopes with wind-on were corrected using the wind-off curve-fitted data. A procedure was incorporated into the UPWT VMD image processing to provide a better spatial mapping of the wind-on and wind-off images in a manner similar to the image registration process used in the PSP technique (reference 8). For example, the wind-on model angle of attack computed by the wind tunnel data system consisted of the main support system accelerometer measurement, the deflections of the model, balance, and sting caused by aerodynamic loads, and the tunnel flow angle. However, to achieve the same angle of attack during wind-off conditions required the main support system to be set to a higher angle such that the model spatial location differed relative to the wind-on case. Consequently, the wind-off tare that was applied was determined at an angle of attack that did not include the sting deflection angles or the tunnel flow angle, which significantly improved the spatial alignment with the corresponding wind-on image.

The final wind-on VMD local angle of attack at each target row was subsequently computed as the uncorrected wind-on angle of attack

minus the static tare plus the flow angle at a given Mach number and Reynolds number. The local twist was computed as the difference between the VMD-measured angle of attack at a given target row and the model angle of attack computed by the wind tunnel data system. The resultant data file was then transferred to a separate computer workstation for conversion to binary format suitable for use in a Data Engineering Scripting Language (DESL) software package for final plotting and analysis (reference 17).

Discussion of Results

The primary application of the UPWT VMD system in the current investigation was to determine local wing twist. Secondary measurements included wing deflections or bending, which are not presented in this report.

Flapped Wing

Span Station Sweeps

Figures 14-18 are composite plots of the variation of the measured wing twist angle, θ, versus the model angle of attack, α, at all span stations (η = 0.226, 0.411, 0.541, 0.760, and 0.991) corresponding to a unit Reynolds number of 4.0 x 10^6 and Mach numbers of 1.6, 1.8, 2.1, 2.4, and 2.7, respectively. Negative values of the wing twist correspond to leading edge down. Error bars are superimposed on each data point corresponding to the 95 percent confidence limits based on the Student's *t* distribution (reference 18) and a sample size of 30. The wing twist at η = 0.226 is negligible at any Mach number, since this measurement station is within an essentially rigid region near the wing-fuselage junction. The wing twist measurements at η = 0.411 exhibit a systematic trend with the angle of attack but are typically small, since this station is also within a thicker region of the wing. The wing twist consistently increases at η = 0.541, 0.760, and 0.991, where the reduced section thickness and presence of flap breaks and pressure tubing channels increase the wing flexibility and sensitivity to the aerodynamic loading. The trends are similar at all Mach numbers, although the magnitude of the wing twist diminishes with increasing Mach number. The latter effect is shown in more detail in the next section.

Mach Number Sweeps

Figures 19-23 show the effect of the Mach number on the wing twist at η = 0.226, 0.411, 0.541, 0.760, and 0.991, respectively. The unit Reynolds number is constant at 4.0 x 10^6. The wing twist is insensitive to the Mach number at η = 0.226 because of the rigid properties of the wing at this station. Similarly, the Mach number effect on the wing twist at η = 0.411 is small. The negative slopes of the wing twist curves at η = 0.541, 0.760, and 0.991 are less pronounced as the Mach number increases. At η = 0.991 (figure 23), for example, the wing twist angle decreases from a maximum of approximately -2.6 degrees at M_∞ = 1.60 to approximately -1.2 degrees at M_∞ = 2.70. Part of this effect is attributed to the decreased free-stream dynamic pressure at the higher Mach numbers (M_∞ = 2.4 and 2.7, for example). However, the majority of the effect is caused by the reduced aerodynamic loads as the Mach number increases from the lower to higher supersonic conditions (reference 19).

Reynolds Number/Dynamic Pressure Sweeps

Figures 24-28 show the wing twist at η = 0.226, 0.411, 0.541, 0.760, and 0.991, respectively, at a Mach number of 2.1 and unit Reynolds numbers of 1.0, 2.0, 3.0, 4.0 and 5.0 x 10^6. The Reynolds number effect is confounded with the free-stream dynamic pressure, *q*, since UPWT cannot conduct Reynolds number sweeps at constant *q*. The most significant effects are observed at η = 0.541, 0.760, and 0.991, where a five-fold increase in the Reynolds number and dynamic pressure generally promotes a five-fold increase in the wing twist angle at a given angle of attack.

Data Repeatability

Figures 29-33 compare the wing twist angles obtained at η = 0.226, 0.411, 0.541, 0.760, and 0.991, respectively, in three repeat runs at a Mach number of 2.1 and a unit Reynolds number of 4.0 x 10^6. The repeat runs were obtained within the same wind-on run series. The lower plot in each figure compares the wing twist angle versus the angle of attack obtained in the three repeat runs. The upper plot in each figure shows the differences in the twist angles, where the delta-twist values ($\Delta\theta$) were obtained by applying a third-order polynomial curve fit to the original data, interpolating in each run to the nominal values of the independent variable, then averaging and subtracting the averages from the interpolated data. The results suggest good short-term repeatability of the wing twist measurements, and the $\Delta\theta$ values are typically bounded by upper and lower limits corresponding to +/-0.02 degrees or less. These results are consistent with previous VMD testing cited in references 1-6.

Solid Wing

For completeness, the wing twist measurements obtained on the solid wing model are presented in the following sections. Reynolds number/dynamic pressure sweeps and data repeatability runs were not performed on the solid wing model.

Span Station Sweeps

Figures 34-38 are composite plots of the variation of the measured wing twist angle versus the model angle of attack at all span stations (η = 0.226, 0.411, 0.541, 0.760, and 0.991) corresponding to a unit Reynolds number of 4.0 x 10^6 and Mach numbers of 1.6, 1.8, 2.1, 2.4, and 2.7, respectively. The wing twist angles are negligible at η = 0.226 and very small (less than 0.2 degrees) at η = 0.411 and 0.541 at any Mach number. These results are indicative of the more rigid wing construction compared to the flapped wing model. The more significant wing twist angles are confined to the outer span stations, η = 0.760 and 0.991, where the wing is sufficiently thin to render it sensitive to deformation due to aerodynamic loads. Similar to the results obtained on the flapped wing, the wing twist trends with the angle of attack at a given span station are insensitive to the Mach number, although the magnitude of the wing twist diminishes with increasing Mach number.

Mach Number Sweeps

Figures 39-43 show the effect of the Mach number on the wing twist at η = 0.226, 0.411, 0.541, 0.760, and 0.991, respectively. The unit Reynolds number is constant at 4.0 x 10^6. The wing twist is insensitive to the Mach number at η = 0.226, 0.441, and 0.541 because of the rigid properties of the solid wing at these three stations. The slopes of the wing twist versus angle of attack curves at η = 0.760 and 0.991 exhibit a consistent decrease as the Mach number increases. At η = 0.991 (figure 43), for example, the wing twist angle decreases from a maximum of approximately -1.9 degrees at M_∞ = 1.60 to approximately -0.9 degrees at M_∞ = 2.70.

Comparison of Flapped and Solid Wings

Figures 44-48 compare the measured wing twist angles obtained on the flapped and solid wing models at M_∞ = 1.6, 1.8, 2.1, 2.4, and 2.7, respectively, and a unit Reynolds number of 4.0 x 10^6. Each figure contains comparison plots at η = 0.226, 0.411, 0.541, 0.760, and 0.991. The differences are small at η = 0.226 and 0.441 at any Mach number. At the outer span stations, however, the VMD measurements clearly show the more flexible response of the flapped wing compared to the solid wing.

Figures 49-53 show composite plots of the computed differences between the flapped wing and the solid wing, $\Delta\theta$, at all span stations and at M_∞ = 1.6, 1.8, 2.1, 2.4, and 2.7, respectively. The unit Reynolds number is constant at 4.0 x 10^6. Third-order polynomial curve fits were applied to the original wing twist data, and the differences between the interpolated values

of the wing twist were calculated in 0.5-degree increments in the model angle of attack. Each figure reveals two distinct subsets consisting of small differences in the wing twist angle at η = 0.226 and 0.411 and much larger differences at η = 0.541, 0.760, and 0.991. The largest differences in the wing twist angles between the flapped and solid wings typically occur at η = 0.760 at a given Mach number. The wing tip regions of both wings are quite thin and flexible, which accounts for the diminished $\Delta\theta$ values at η = 0.991. The increased variability of the $\Delta\theta$ curves at M_∞ = 2.4 and 2.7 in figure 52 and figure 53, respectively, are attributed to a higher turbulence level in operating mode 1-II in Test Section 1 (reference 10). However, the $\Delta\theta$ trends are consistent with the results obtained at the lower supersonic Mach numbers in operating mode 1-IA.

Summary

A dedicated video model deformation system was established at the NASA LaRC UPWT to measure wing twist at supersonic speeds. The VMD system was successfully applied to the measurement of wing twist on two precision metal models of a supersonic transport airplane configuration. The models featured identical outer mold lines. However, the wings of one model were more flexible because of the presence of multiple leading- and trailing-edge flap segments and internal machined channels to accommodate surface static pressure instrumentation. The second model featured single-piece, solid-construction wings. The VMD system effectively quantified the sensitivity of the local wing twist to the free-stream Mach number and a combined effect of the Reynolds number and free-stream dynamic pressure in a repeatable manner. In addition, the wing twist measurements clearly illustrated the more significant aeroelastic deformation of the flapped wing at the mid- and outer-span measurement stations which were most affected by the presence of the segmented flaps and the internal pressure tubing channels. The VMD system was demonstrated to be an effective, end-to-end optical measurement tool featuring the installation, in-situ calibration, and image acquisition, processing, and analysis by resident wind tunnel facility personnel.

References

1. Burner, A. W. and Martinson, S. D., "Automated Wing Twist and Bending Measurements Under Aerodynamic Load," AIAA-1996-2253, June 1996.

2. Burner, A. W., Wahls, R. A., and Goad, W. K., "Wing Twist Measurements at the National Transonic Facility," NASA TM 110229, February 1996.

3. Burner, A. W., "Model Deformation Measurements at NASA Langley Research Center." *AGARD 81st Fluid Dynamics Panel Symposium on Advanced Aerodynamic Measurement Technology*, September 1997.

4. Burner, A. W., Radeztsky, R. H., and Liu, T., "Videometric Applications in Wind Tunnels," *Videometrics V, Proceedings of the International Society for Optical Engineering (SPIE)*, Vol. 3174, pp 234-247, July 1997.

5. Burner, A. W. and Liu, T., "Videogrammetric Model Deformation Measurement Technique," *Journal of Aircraft*, Vol. 38. No. 4, pp 745-754, July-August 2001.

6. Burner, A. W., Liu, T., Garg, S., Ghee, T. A., and Taylor, N. J., "Aeroelastic Deformation Measurements of Flap, Gap, and Overhang on a Semispan Model," AIAA-2000-2386, June 2000.

7. Burner, A. W., Fleming, G. A., and Hoppe, J. C., "Comparison of Three Optical Methods for Measuring Model Deformation," AIAA-2000-0835, January 2000.

8. Erickson, G. E., "Overview of Selected Measurement Techniques for Aerodynamics Testing in the NASA Langley Unitary Plan Wind Tunnel," AIAA-2000-2396, June 2000.

9. Bell, J. H. and Burner, A.W., "Data Fusion in Wind Tunnel Testing: Combined Pressure Paint and Model Deformation Measurements," AIAA-1998-2500, June 1998.

10. Jackson, C. M. Jr., Corlett, W. A., and Monta, W. J., "Description and Calibration of the Langley Unitary Plan Wind Tunnel," NASA TP 1905, November 1981.

11. Wassum, D. L. and Hyman, C. E. Jr., "Procedures and Requirements for Testing in the Langley Research Center Unitary Plan Wind Tunnel," NASA TM 100529, February 1988.

12. Kennelly, R. A. and Goodsell, A., "Skin Friction and Transition Location Measurements on Supersonic Transport Models," Paper No. 160, *9th Millennium International Symposium on Flow Visualization*, August 2000.

13. Cate, K. H., "Videogrammetric Model Deformation Measurement Software Package, Reference Manual for MDef.exe," NASA TM-2001-210554, March 2001.

14. Dismond, H. R., "Videogrammetric Model Deformation Measurement System User Manual," NASA TM-2002-211641, April 2002.

15. Amer, T. R., Liu, T., and Oglesby, D. M., "Characterization of Pressure Sensitive Paint Intrusiveness on Aerodynamic Data," AIAA-2001-0556, January 2001.

16. *Using MATLAB - Version 5*, The MathWorks, Inc., Natick, MA, December 1996.

17. Graham, A. B., "The Data Analysis System, System Description and User's Guide," NASA Langley Research Center, April 1993.

18. Montgomery, D. C., *Design and Analysis of Experiments*, 7th Edition. John Wiley & Sons, Inc., New York, 2009.

19. Küchemann, D., *The Aerodynamic Design of Aircraft*, Pergamon Press, June 1978.

M_∞	Mode	H_o (psfa)	T_o (^oF)	Re/ft	q (psfa)
1.6	1-IA	2157	125	4.0×10^6	909.6
1.8	1-IA	2308	125	4.0×10^6	911.0
2.1	1-IA	656	125	1.0×10^6	221.4
2.1	1-IA	1312	125	2.0×10^6	442.8
2.1	1-IA	1968	125	3.0×10^6	664.2
2.1	1-IA	2623	125	4.0×10^6	885.6
2.1	1-IA	3279	125	5.0×10^6	1107.0
2.4	1-II	3039	125	4.0×10^6	838.2
2.7	1-II	3554	125	4.0×10^6	778.8

Table I. Tunnel operating conditions for VMD testing in UPWT Test Section 1.

Figure 1. Supersonic transport airplane model with retroreflective targets on right wing upper surface for video model deformation testing in the NASA LaRC UPWT.

Figure 2. Aerial view of the NASA LaRC UPWT.

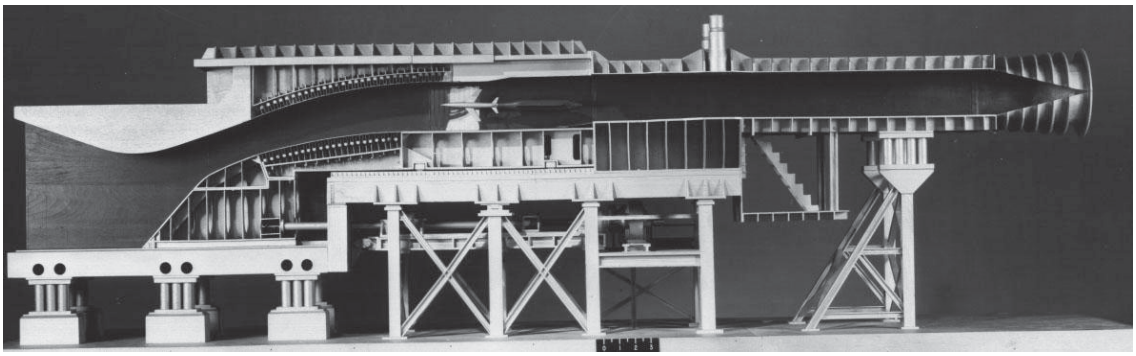

Figure 3. Illustration of UPWT asymmetric sliding nozzle block arrangement.

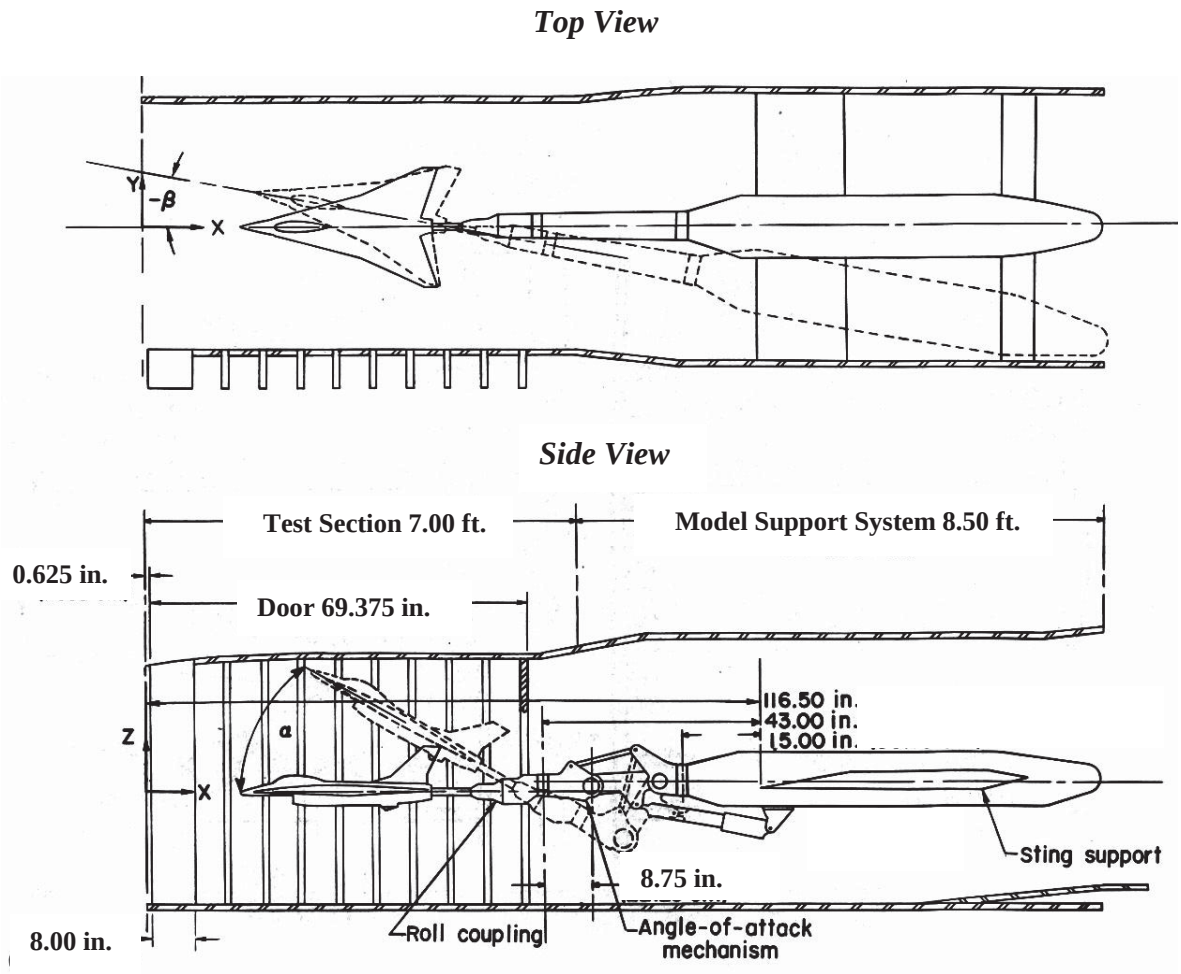

Figure 4. Overall UPWT test section layout.

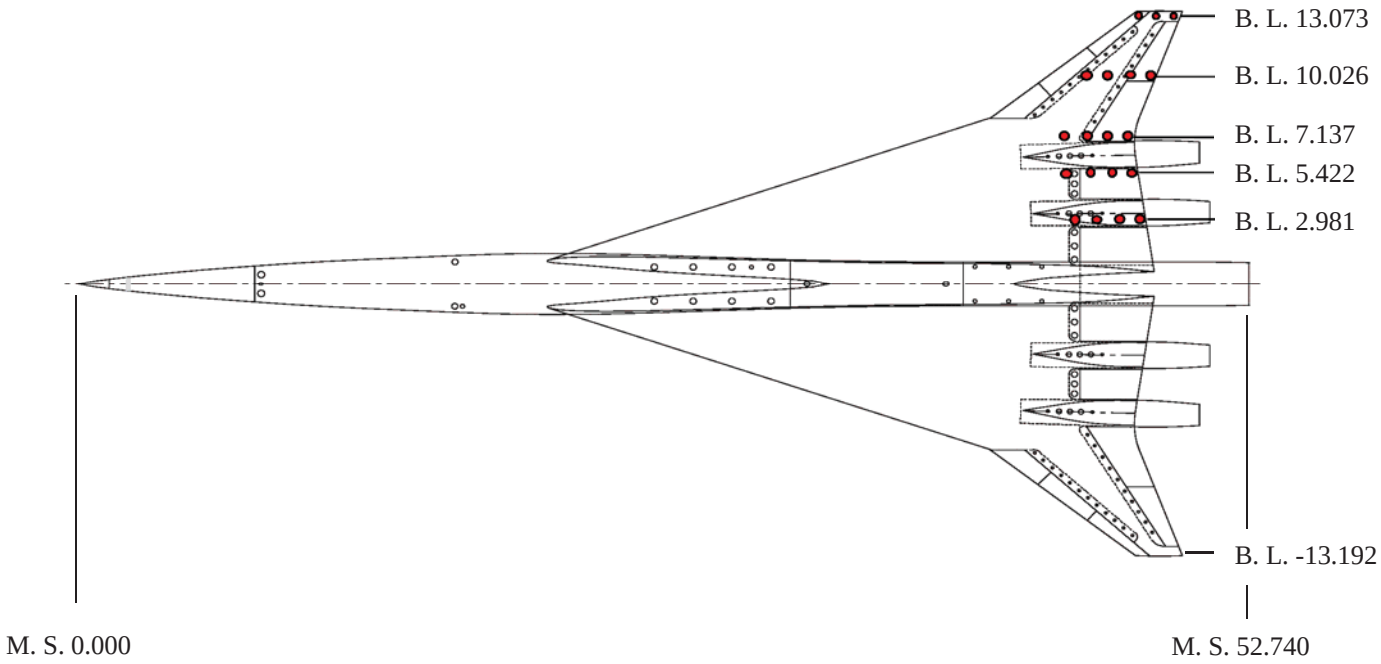

Figure 5. Planview of supersonic transport airplane configuration. (Flapped wing is shown. Retroreflective targets on right wing upper surface are denoted by solid red circles.)

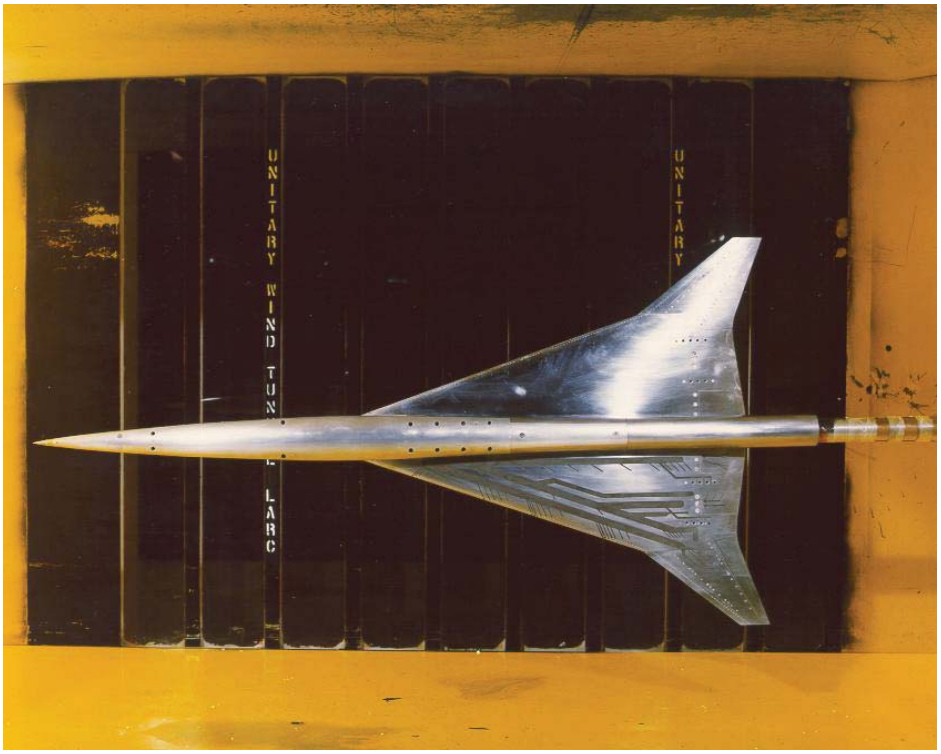

Figure 6. Photograph of flapped wing model installed in UPWT Test Section 1.

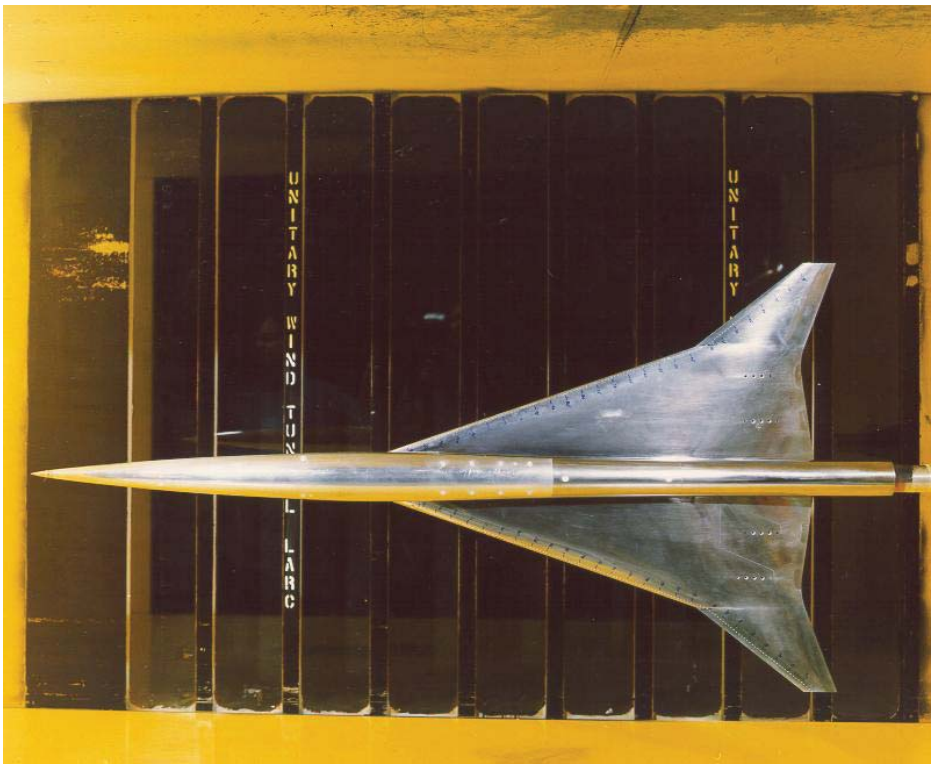

Figure 7. Photograph of solid wing model installed in UPWT Test Section 1.

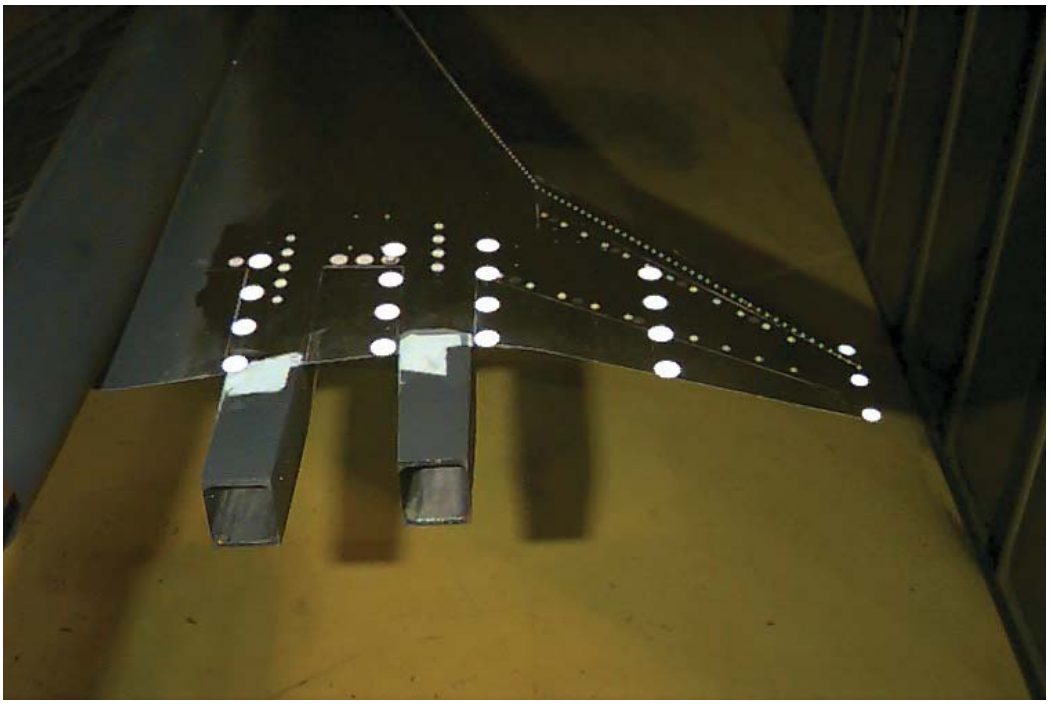

Figure 8. Retrotarget installation on flapped wing model.

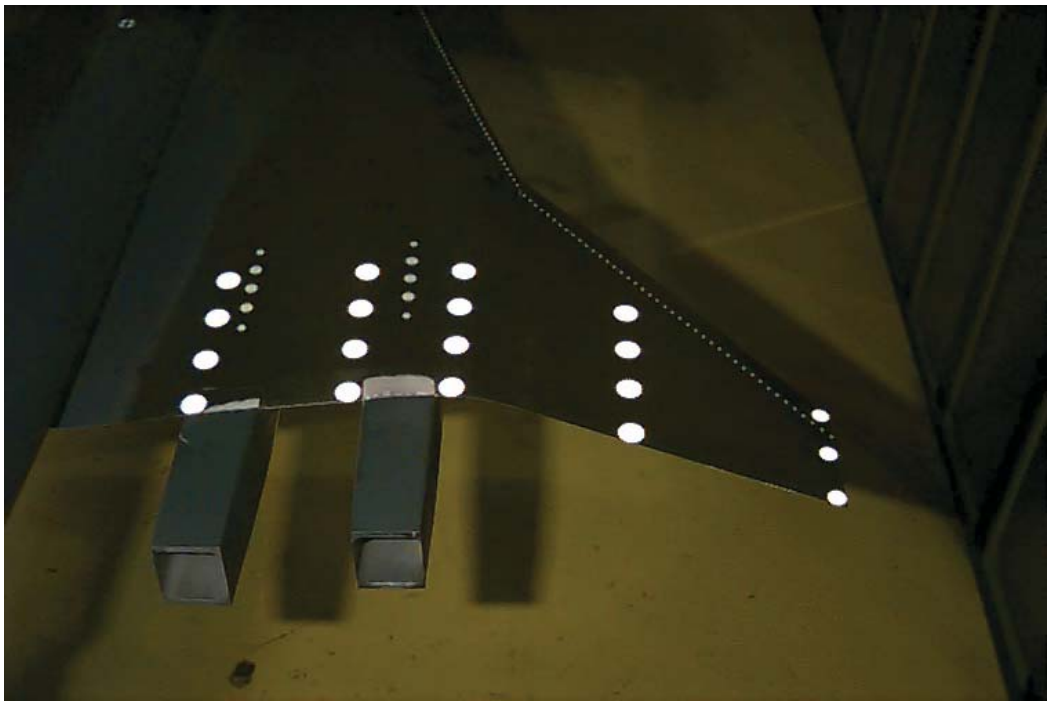

Figure 9. Retrotarget installation on solid wing model.

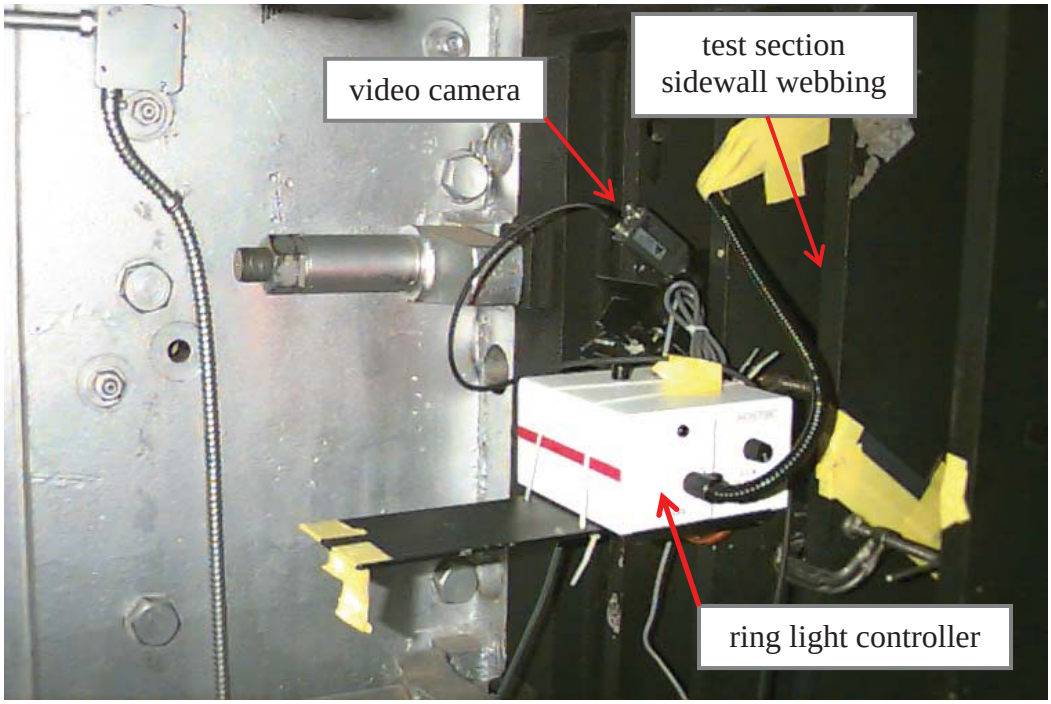

(a) VMD camera installation in webbing of UPWT test section sidewall.

Figure 10. Major components of the UPWT VMD system.

(b) VMD PC workstation in UPWT control room.

Figure 10. Major components of the UPWT VMD system.

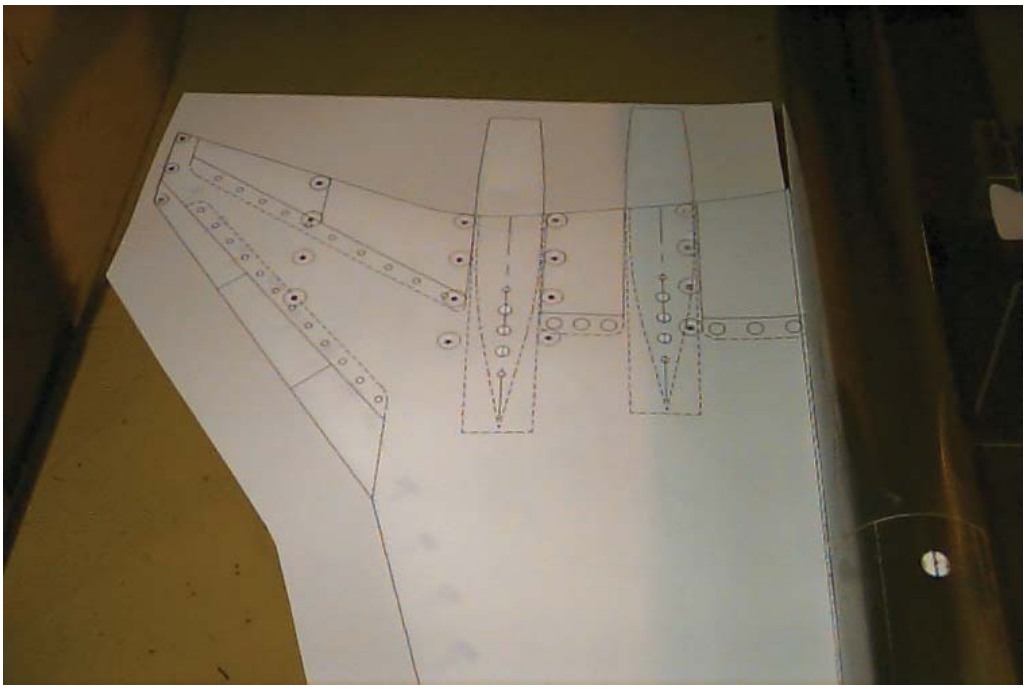

Figure 11. Template for application of retrotargets on right wing upper surface.

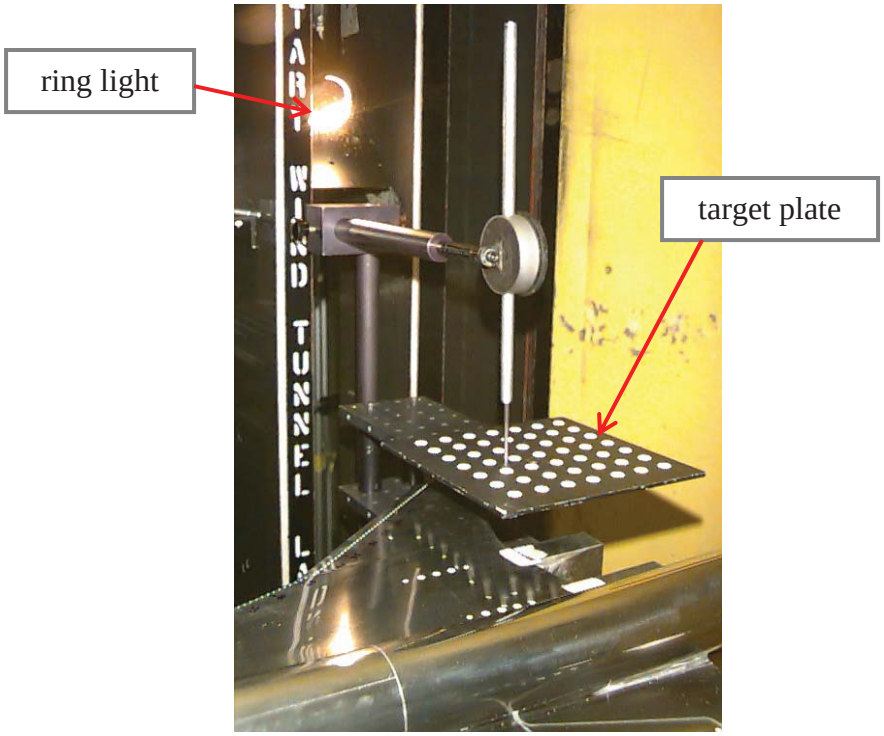

Figure 12. Target plate with 7x7 array of retrotargets for VMD system calibration.

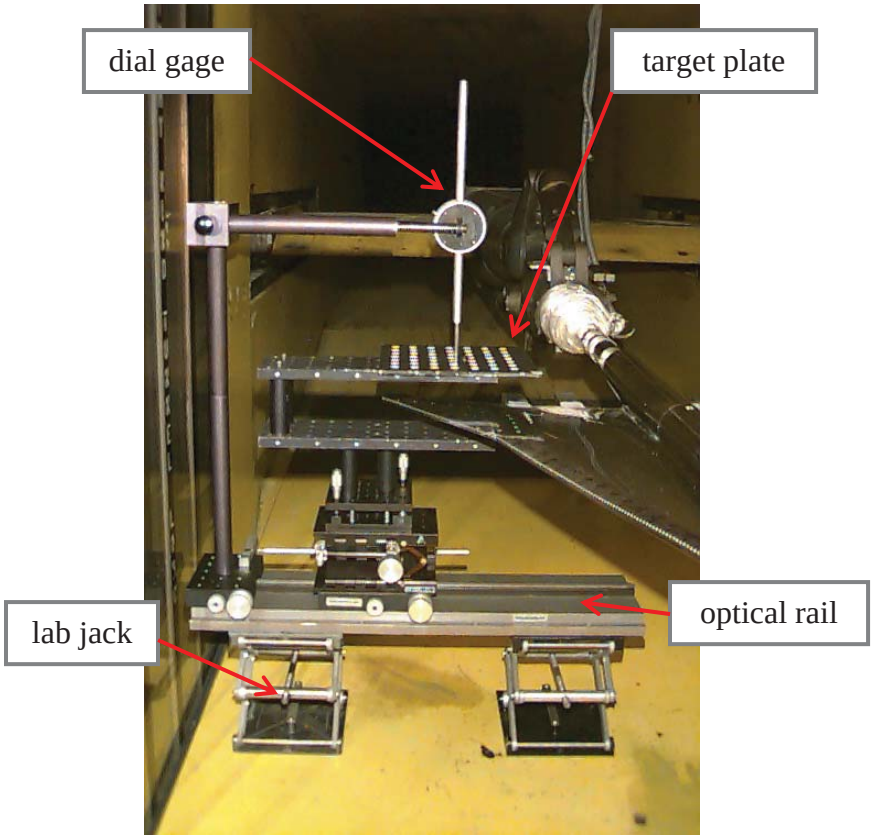

Figure 13. VMD system calibration setup in UPWT Test Section 1.

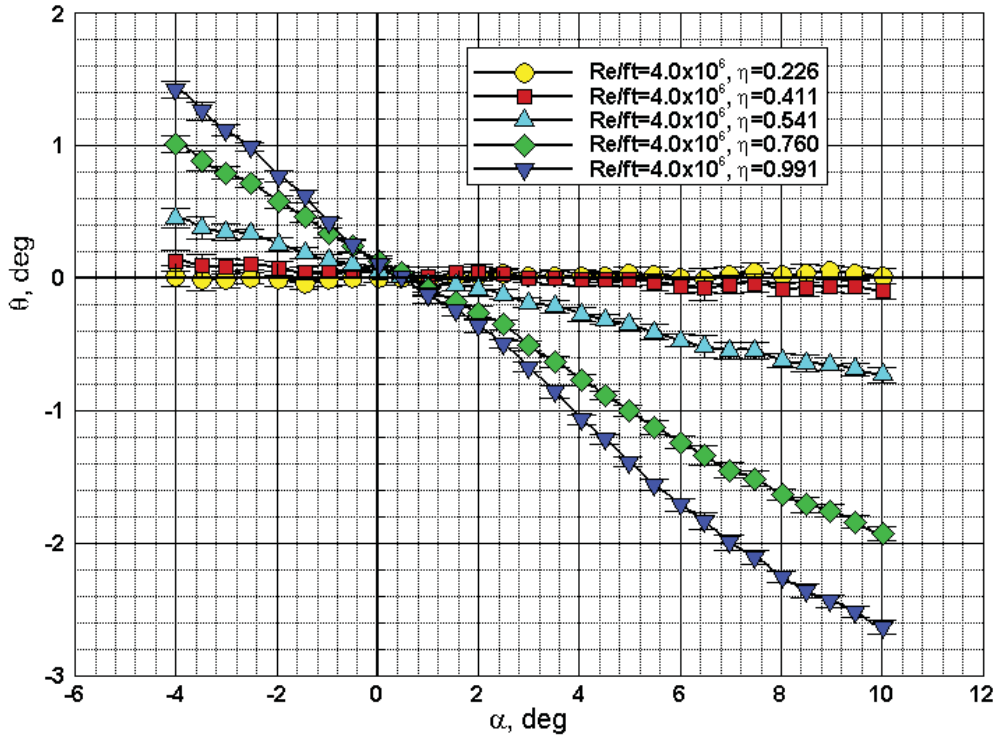

Figure 14. Variation of wing twist with angle of attack at all five measurement stations and $M_\infty = 1.6$; flapped wing.

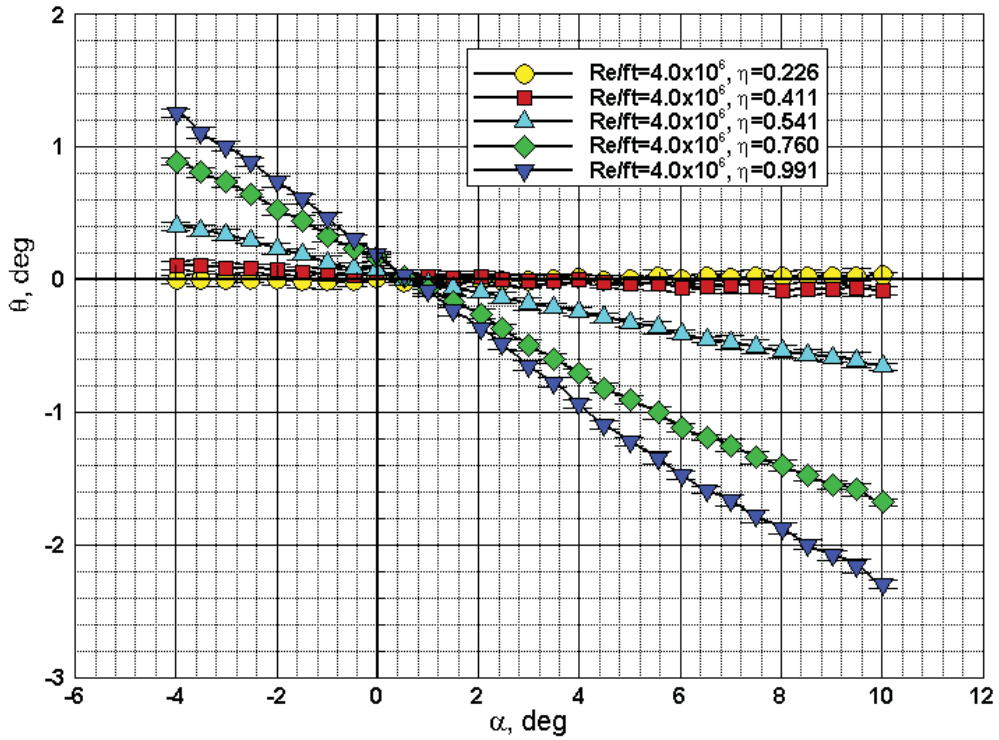

Figure 15. Variation of wing twist with angle of attack at all five measurement stations and $M_\infty = 1.8$; flapped wing.

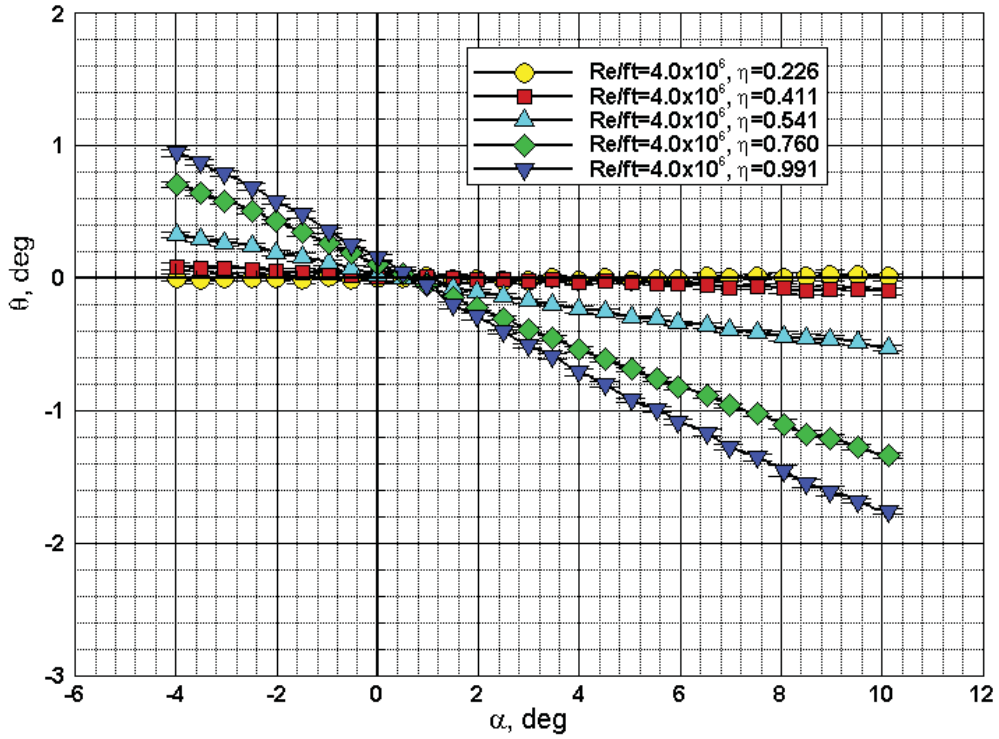

Figure 16. Variation of wing twist with angle of attack at all five measurement stations and $M_\infty = 2.1$; flapped wing.

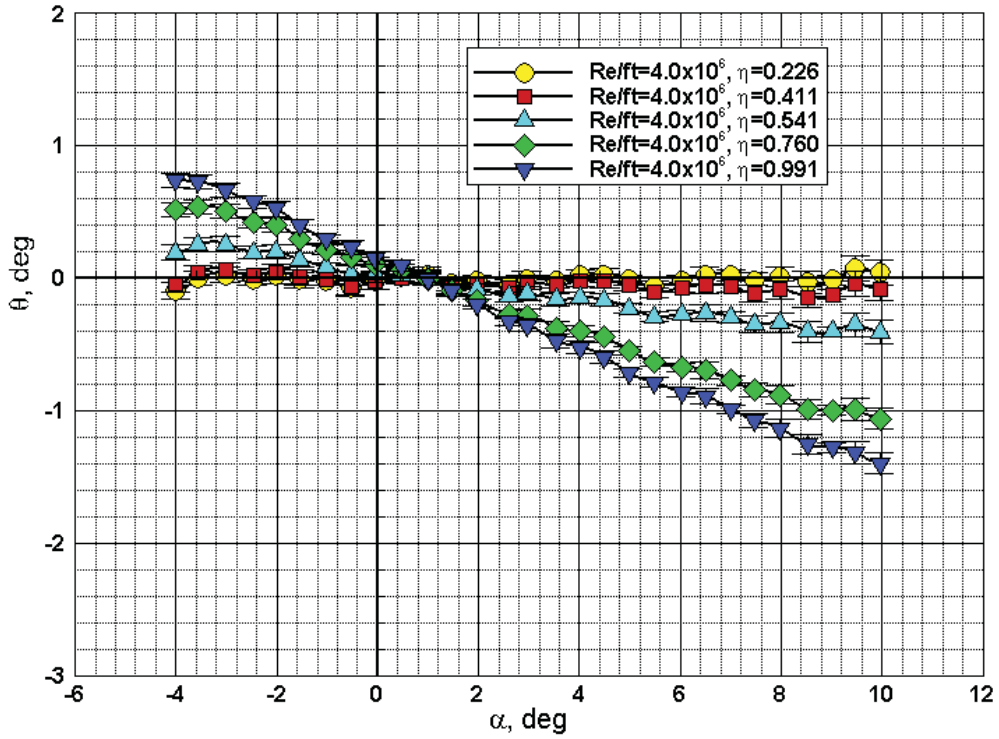

Figure 17. Variation of wing twist with angle of attack at all five measurement stations and $M_\infty = 2.4$; flapped wing.

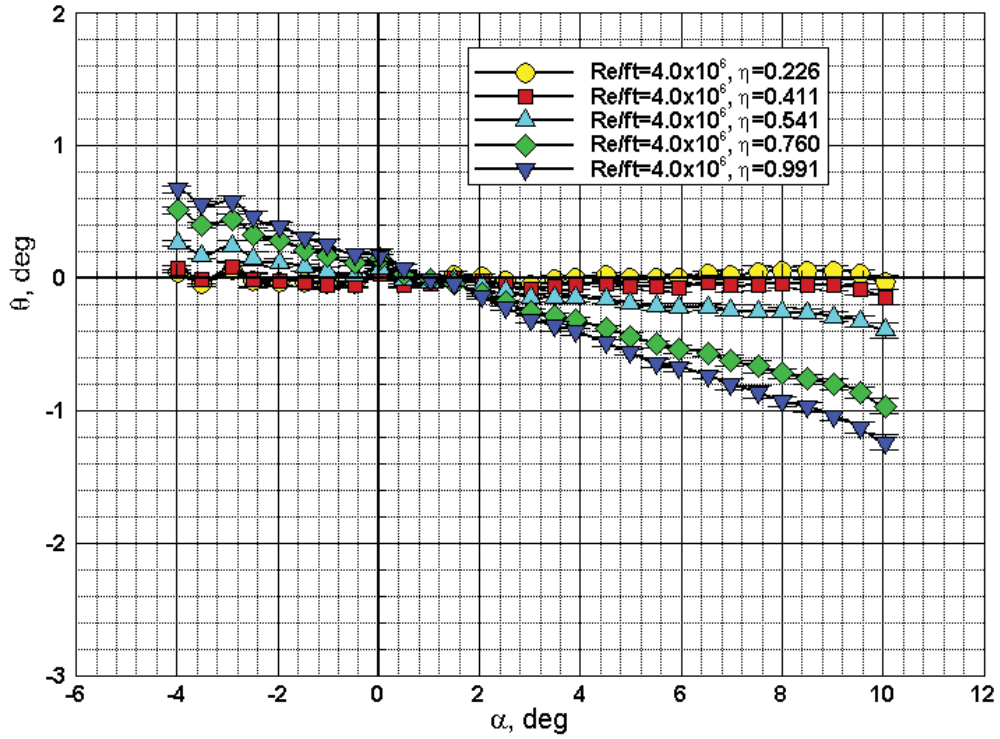

Figure 18. Variation of wing twist with angle of attack at all five measurement stations and $M_\infty = 2.7$; flapped wing.

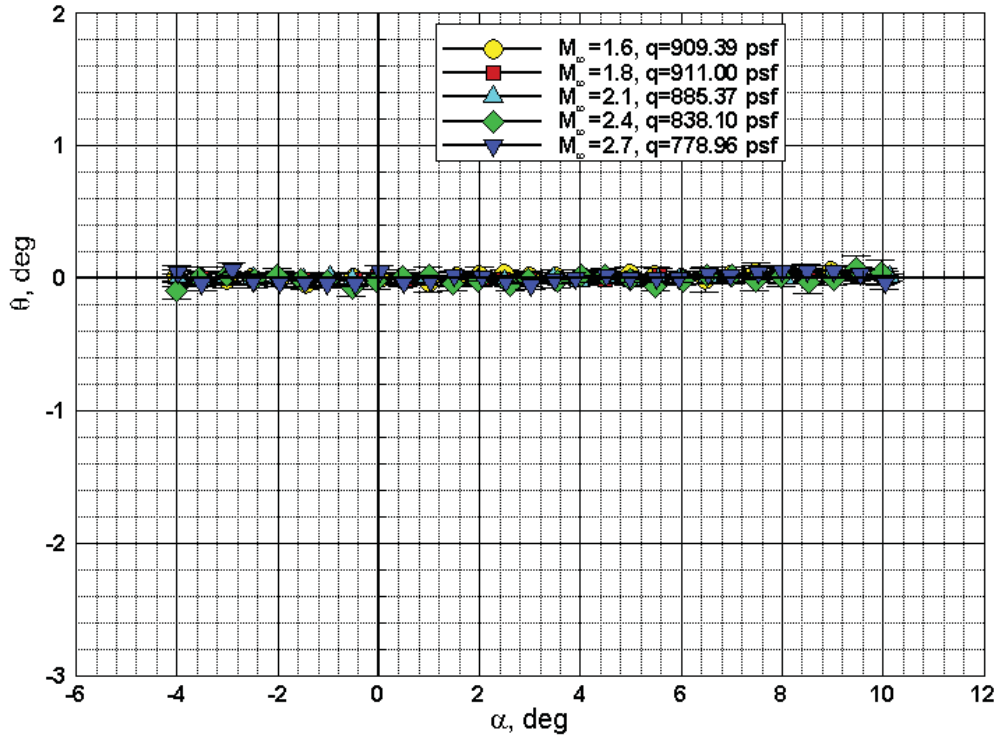

Figure 19. Effect of Mach number on wing twist at Re/ft = 4.0 x10^6 and $\eta = 0.226$; flapped wing.

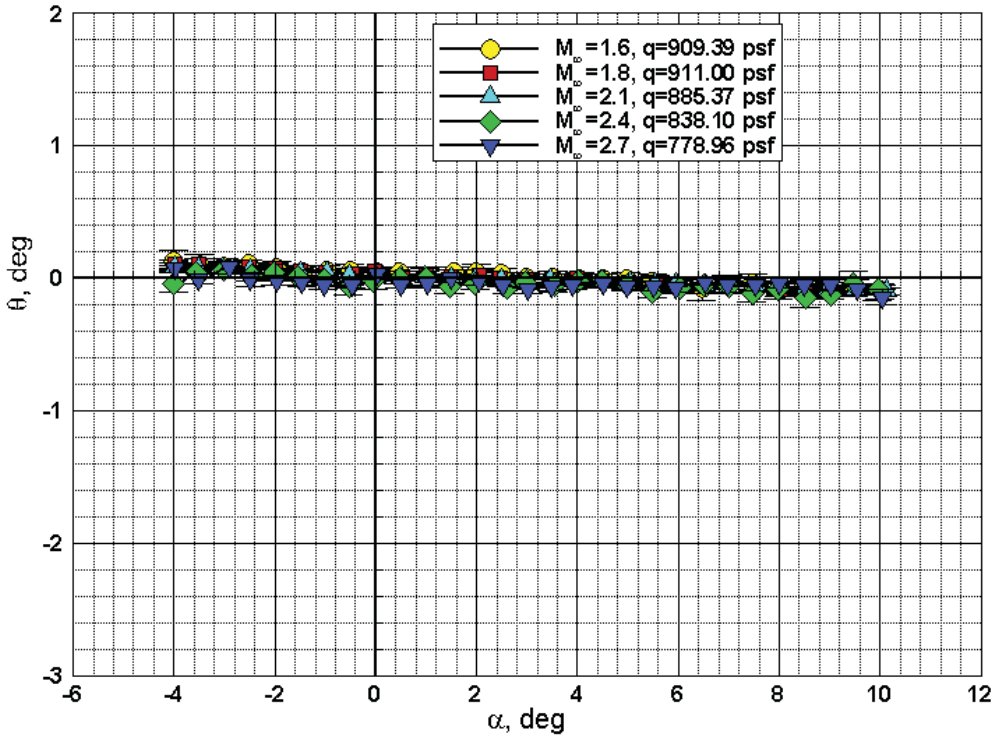

Figure 20. Effect of Mach number on wing twist at Re/ft = 4.0 x10^6 and η = 0.411; flapped wing.

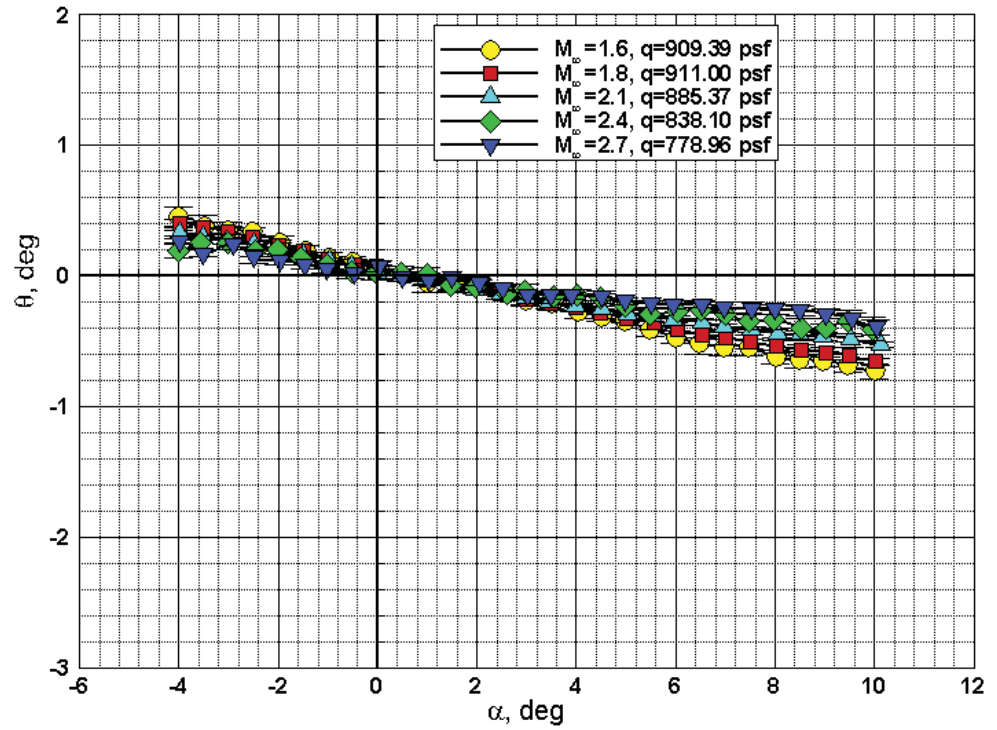

Figure 21. Effect of Mach number on wing twist at Re/ft = 4.0 x10^6 and η = 0.541; flapped wing.

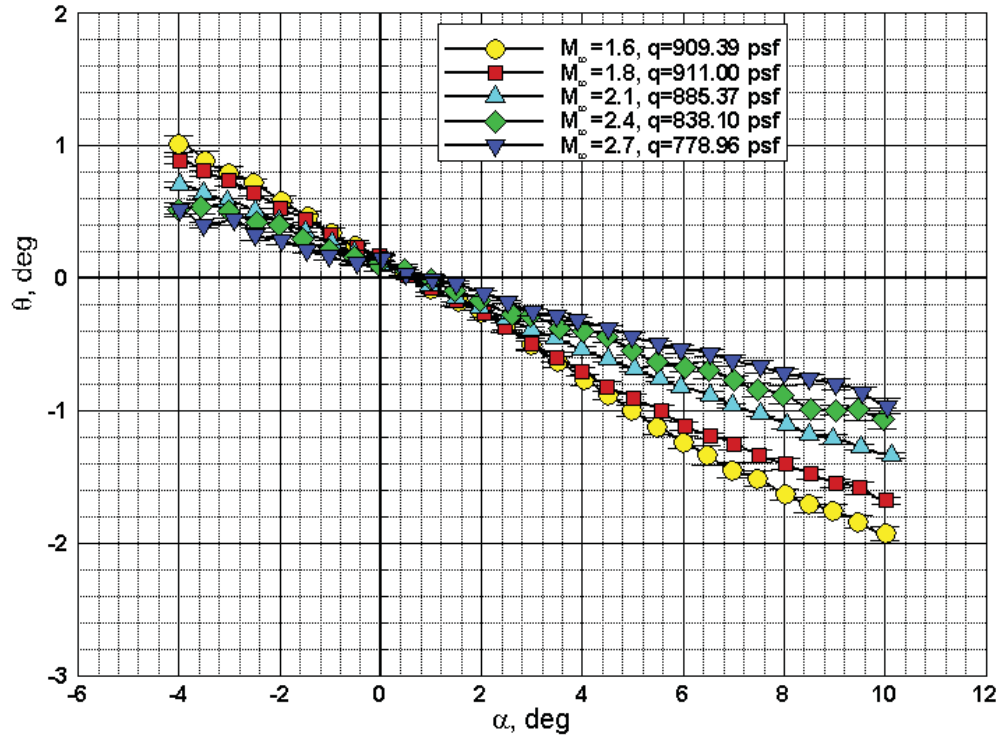

Figure 22. Effect of Mach number on wing twist at Re/ft = 4.0 x10^6 and η = 0.760; flapped wing.

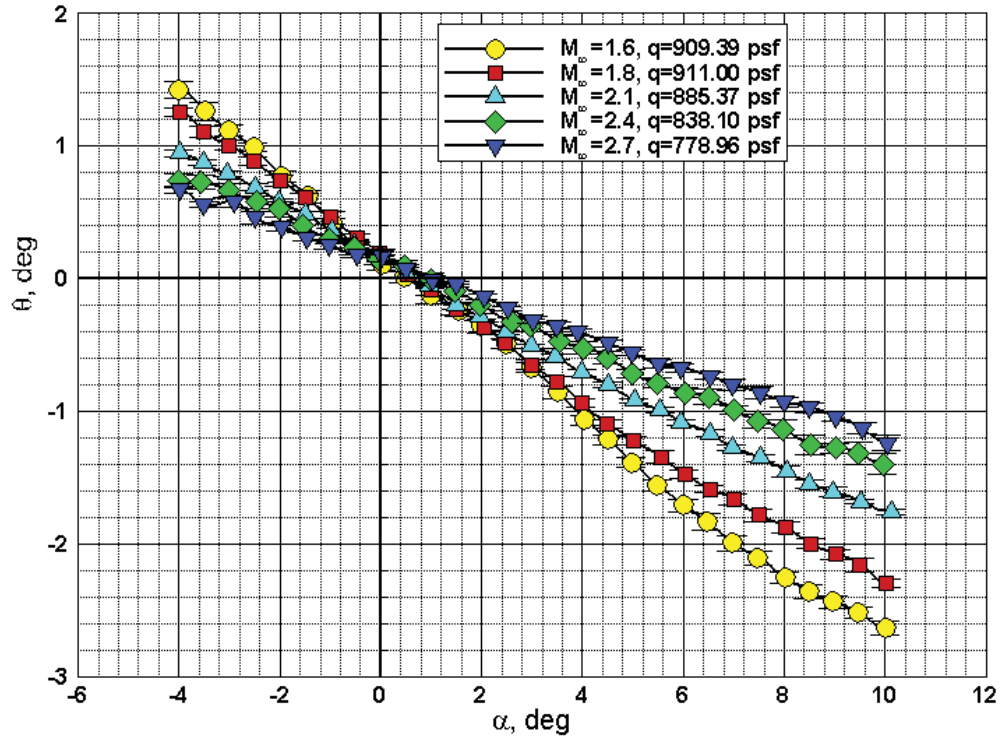

Figure 23. Effect of Mach number on wing twist at Re/ft = 4.0 x10^6 and η = 0.991; flapped wing.

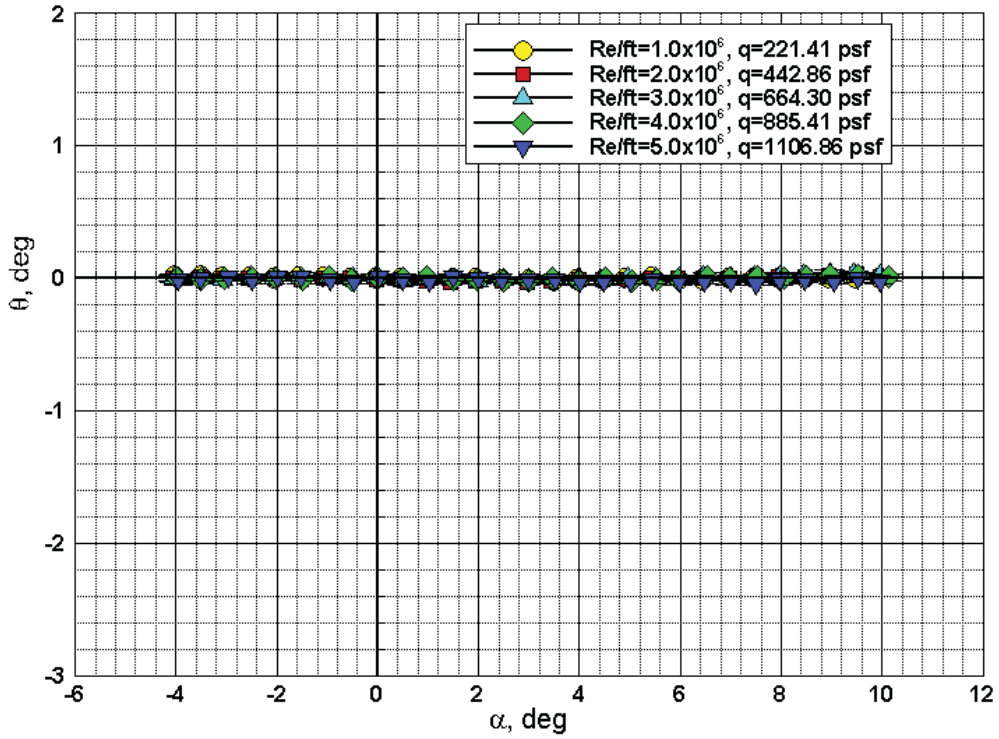

Figure 24. Effect of Reynolds number/dynamic pressure on wing twist at $M_\infty = 2.1$ and $\eta = 0.226$; flapped wing.

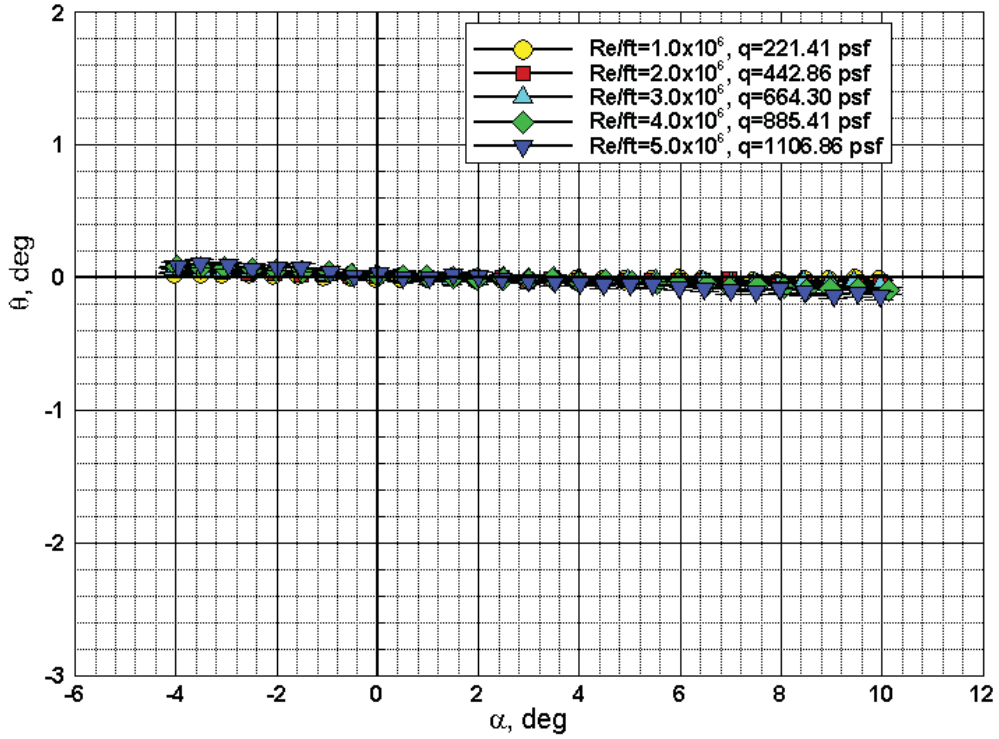

Figure 25. Effect of Reynolds number/dynamic pressure on wing twist at $M_\infty = 2.1$ and $\eta = 0.411$; flapped wing.

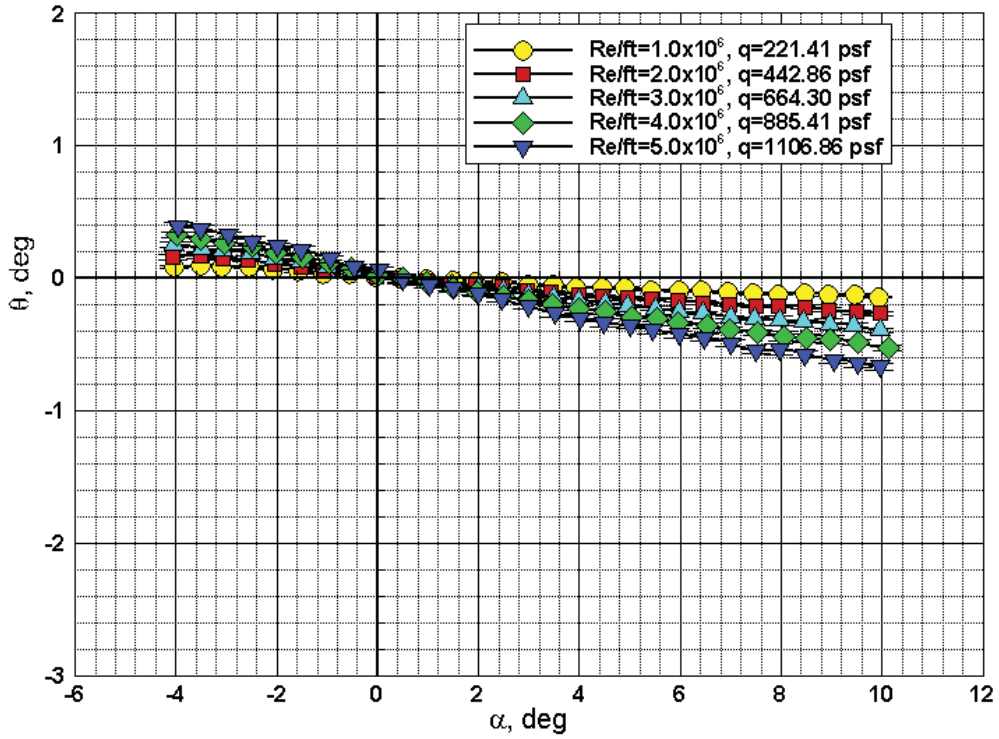

Figure 26. Effect of Reynolds number/dynamic pressure on wing twist at $M_\infty = 2.1$ and $\eta = 0.541$; flapped wing.

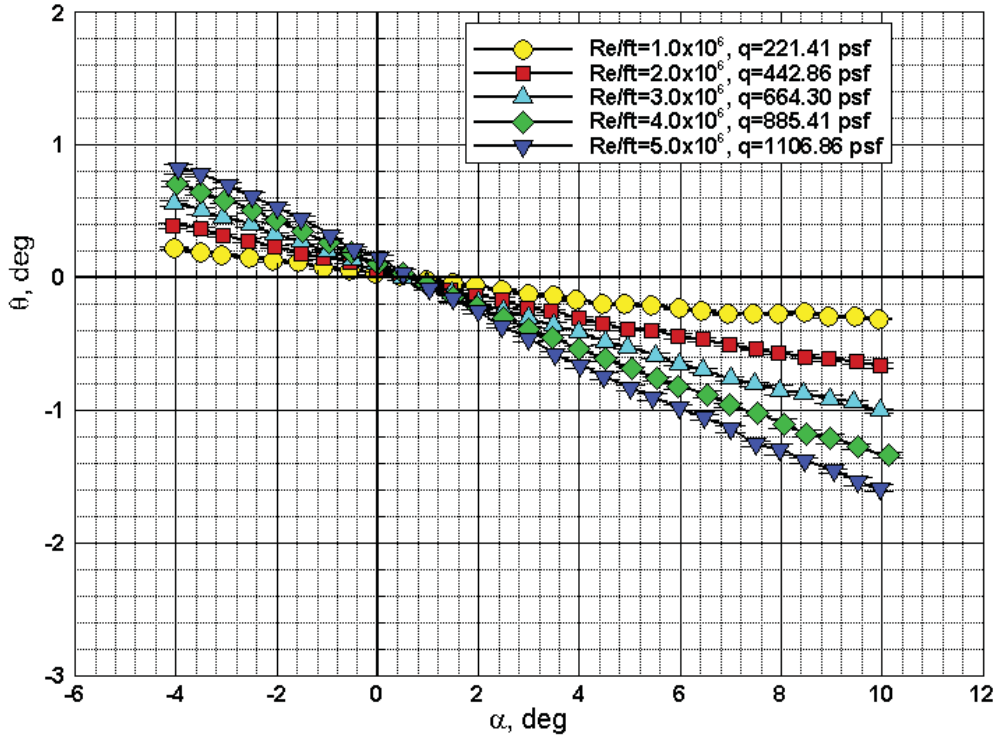

Figure 27. Effect of Reynolds number/dynamic pressure on wing twist at $M_\infty = 2.1$ and $\eta = 0.760$; flapped wing.

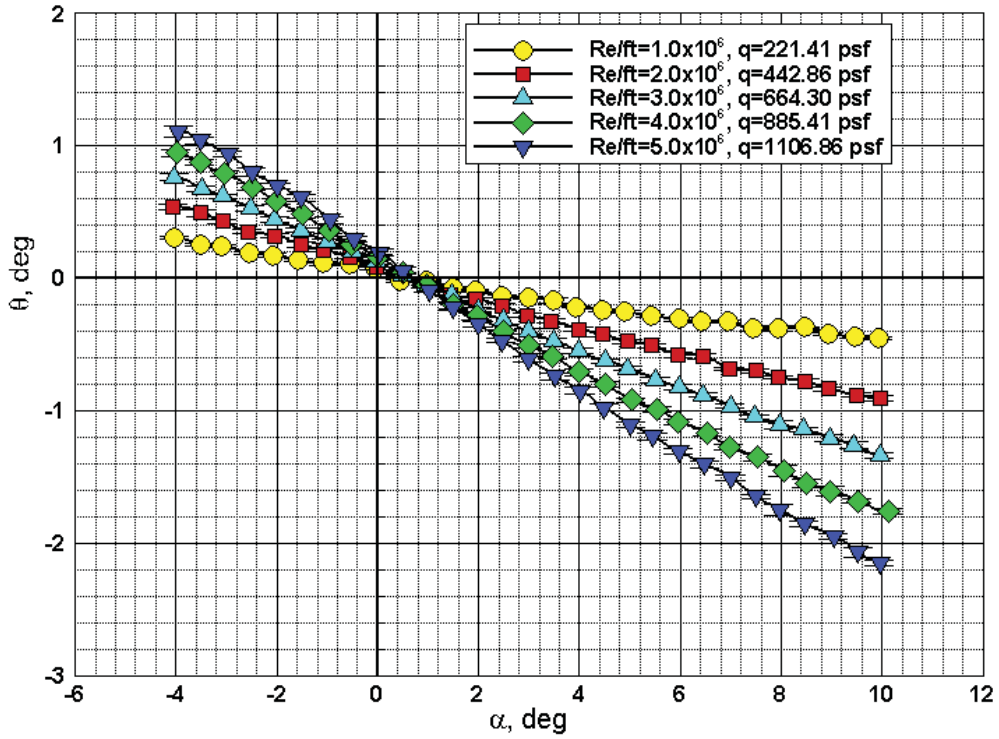

Figure 28. Effect of Reynolds number/dynamic pressure on wing twist at $M_\infty = 2.1$ and $\eta = 0.991$; flapped wing.

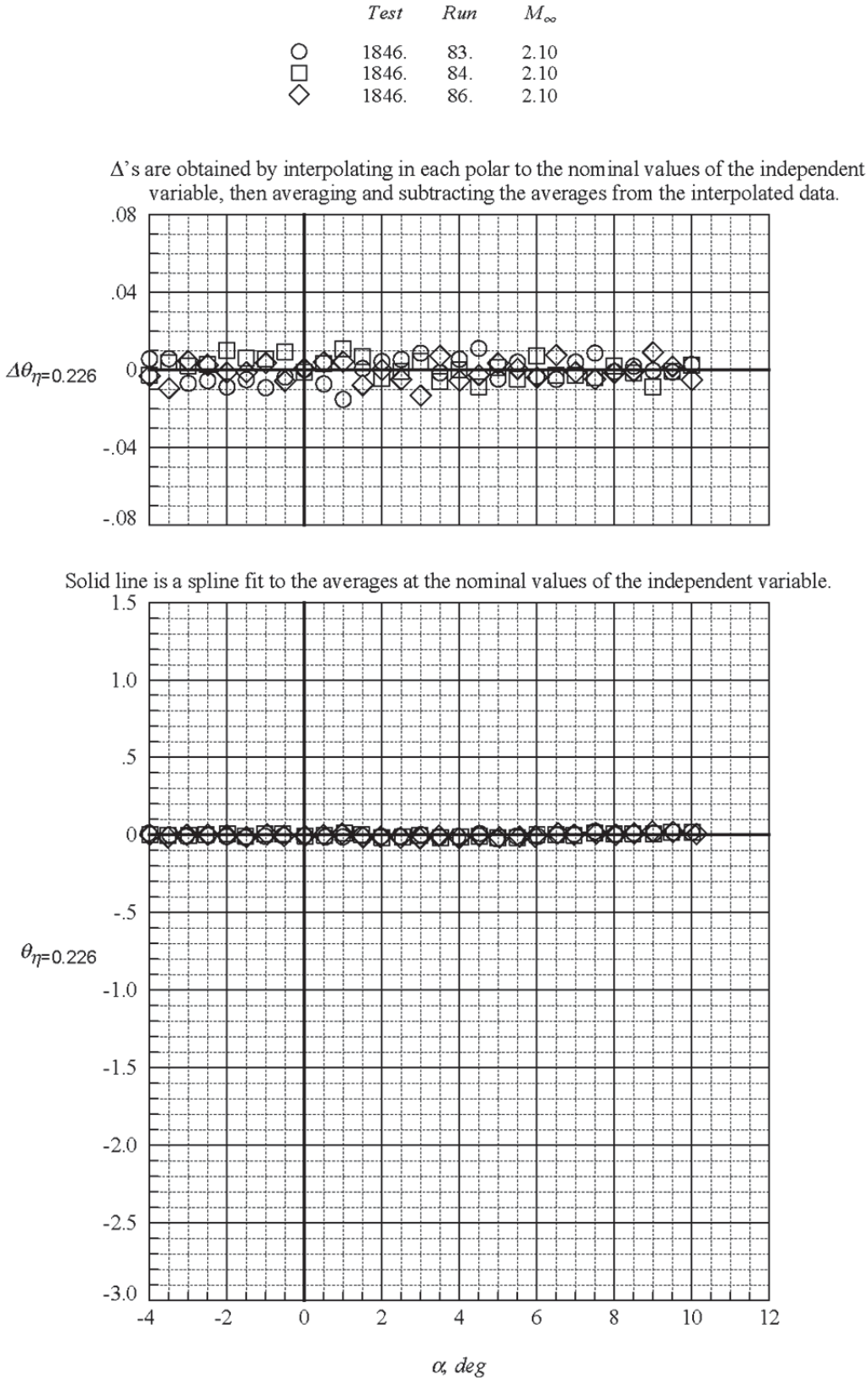

Figure 29. Repeatability of wing twist measurements at M_∞ = 2.1 and Re/ft = 4.0 x 10^6; η = 0.226; flapped wing.

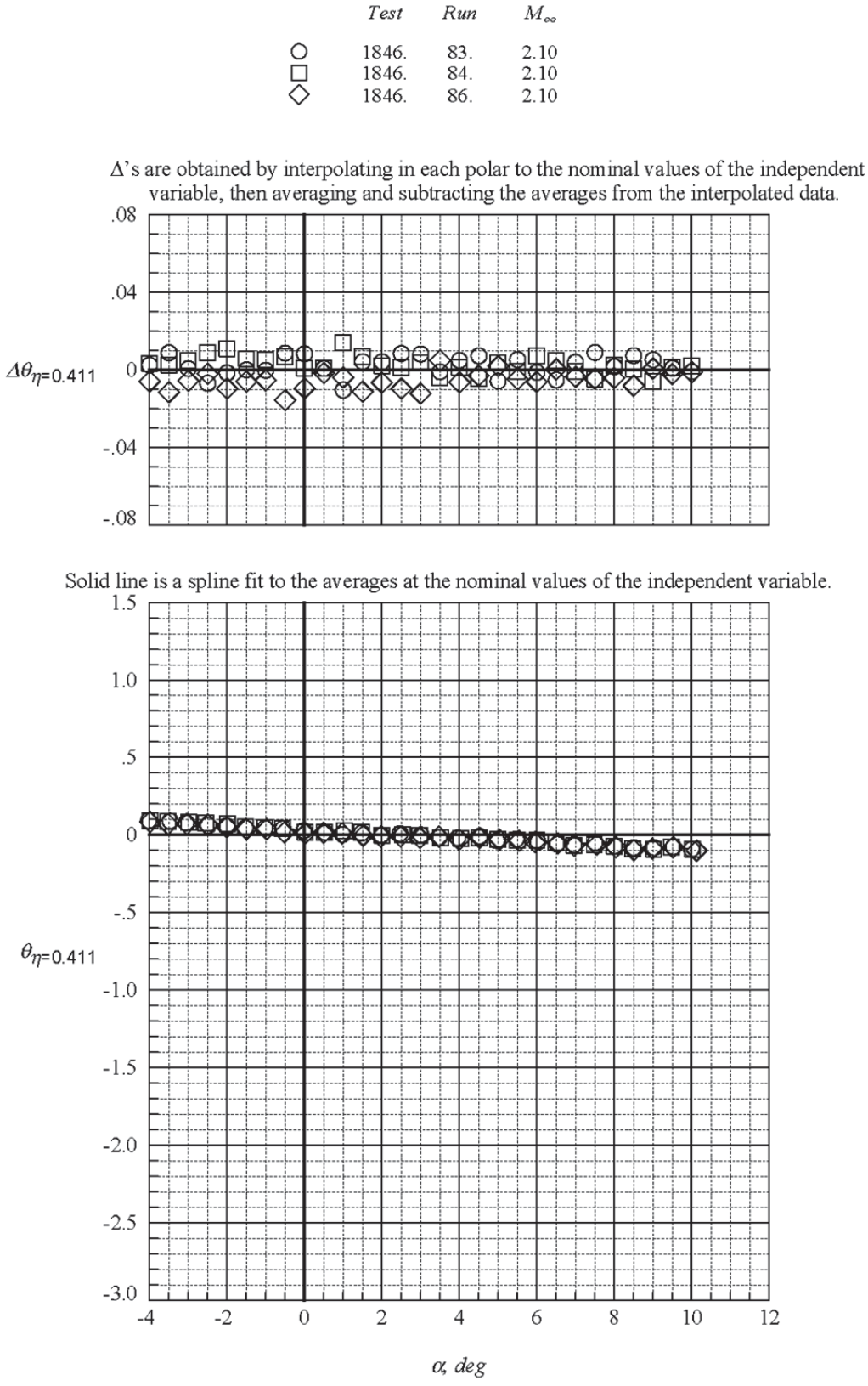

Figure 30. Repeatability of wing twist measurements at M_∞ = 2.1 and Re/ft = 4.0 x 10^6; η = 0.411; flapped wing.

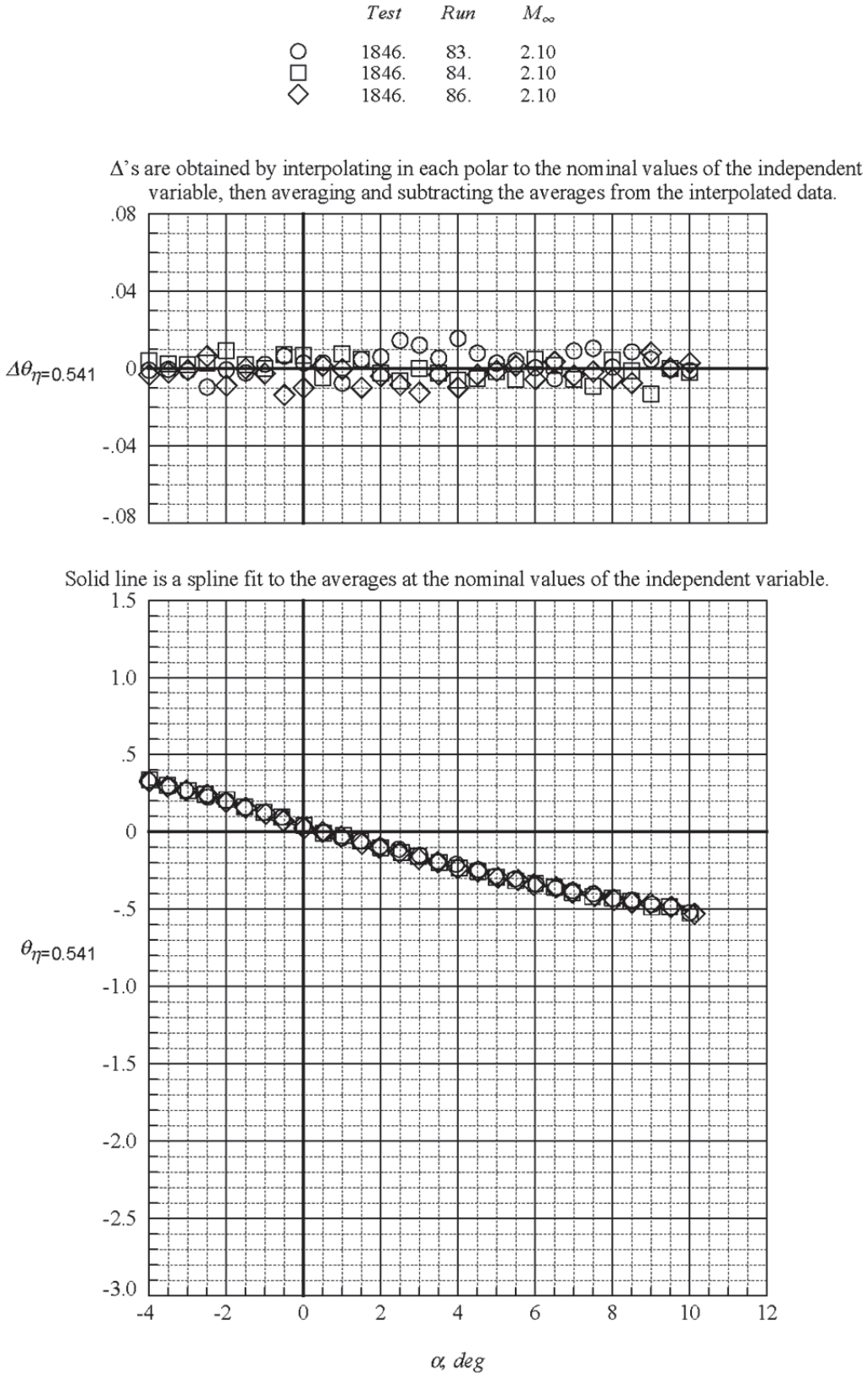

Figure 31. Repeatability of wing twist measurements at M_∞ = 2.1 and Re/ft = 4.0 x 10^6; η = 0.541; flapped wing.

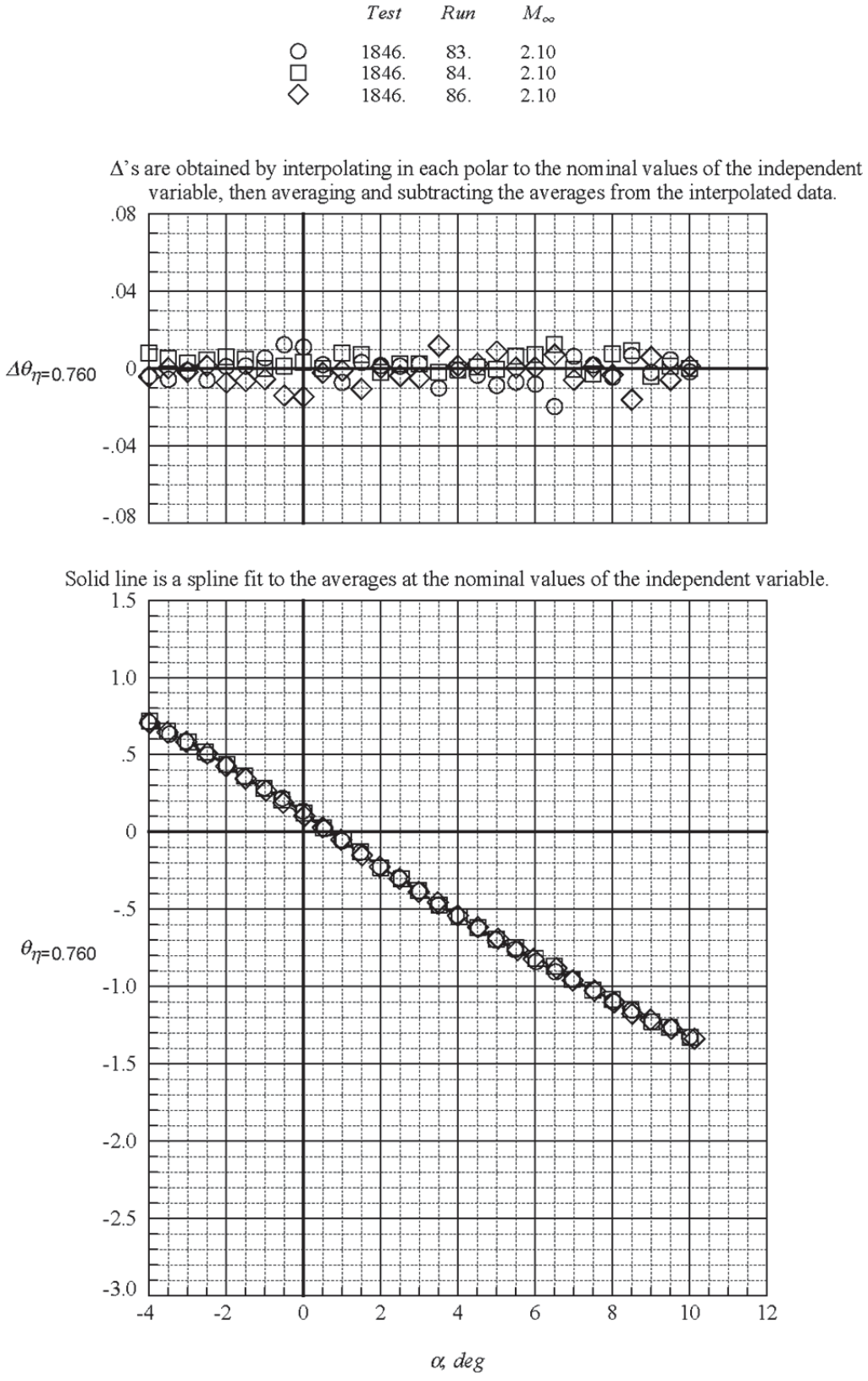

Figure 32. Repeatability of wing twist measurements at M_∞ = 2.1 and Re/ft = 4.0 x 10^6; η = 0.760; flapped wing.

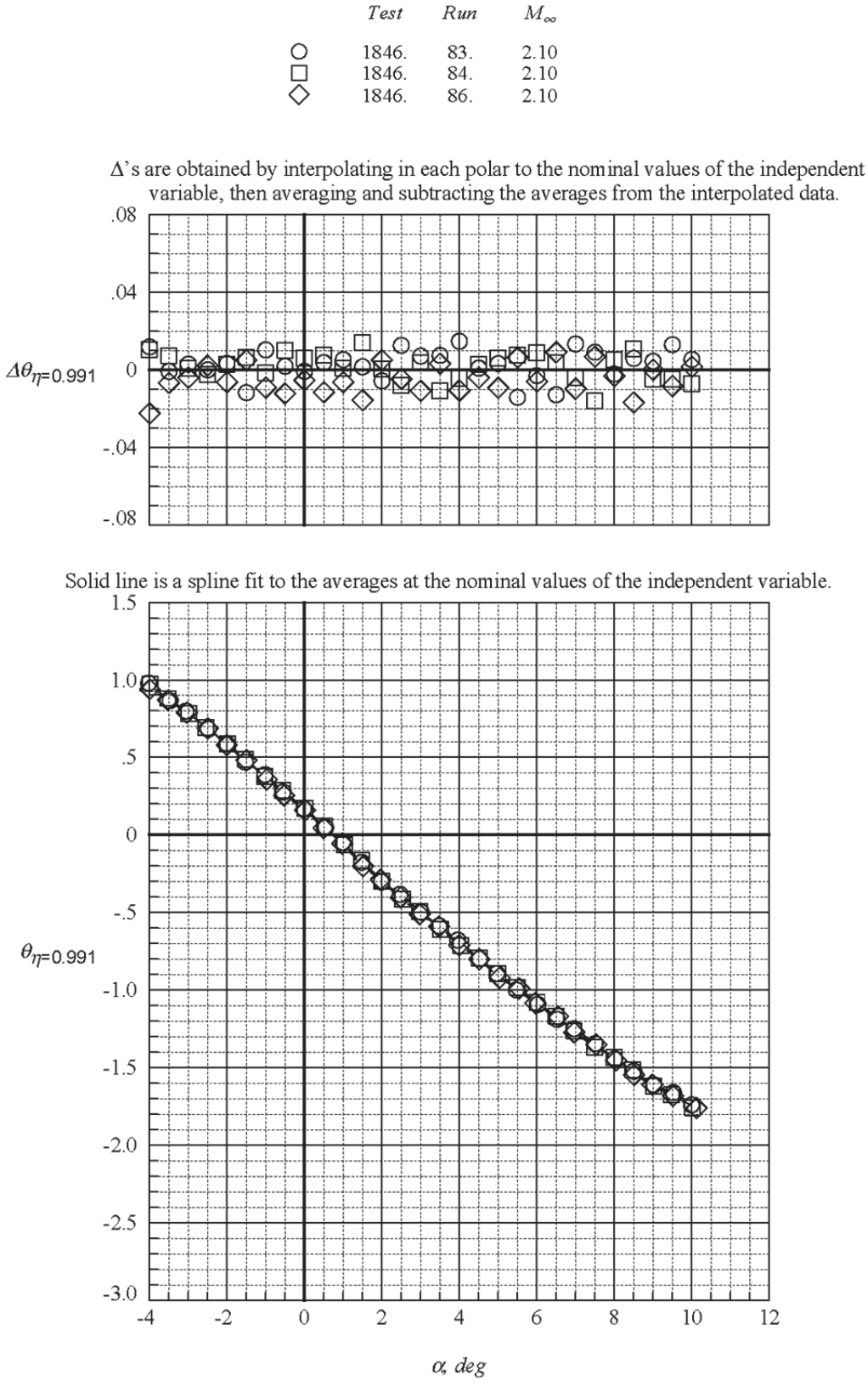

Figure 33. Repeatability of wing twist measurements at M_∞ = 2.1 and Re/ft = 4.0 x 10^6; η = 0.991; flapped wing.

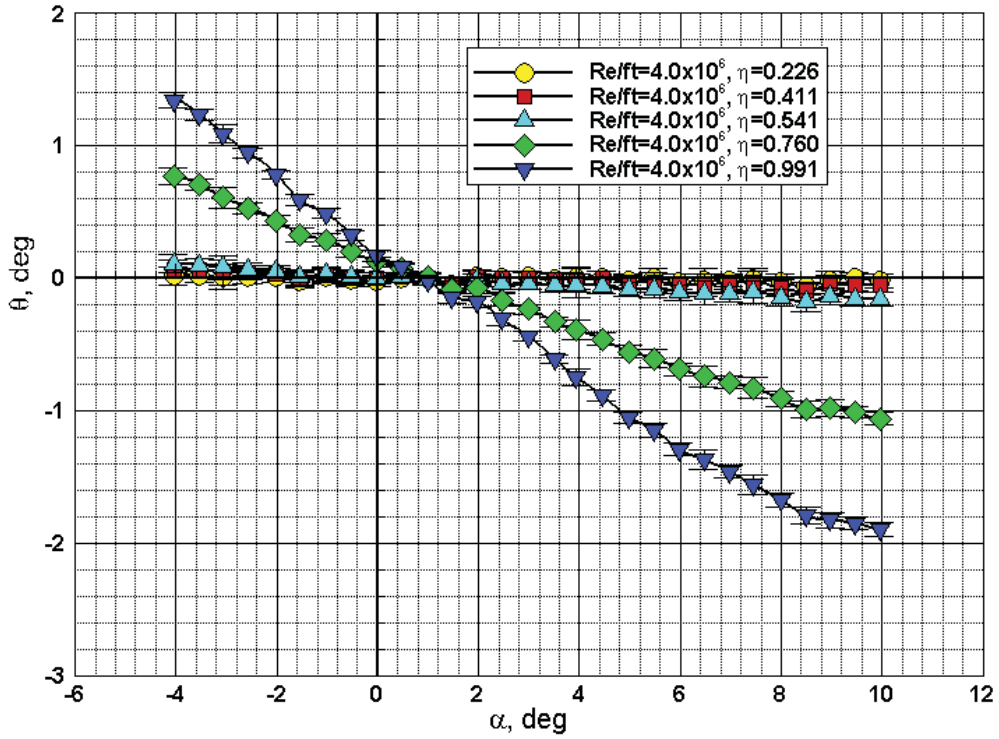

Figure 34. Variation of wing twist with angle of attack at all five measurement stations and $M_\infty = 1.6$; solid wing.

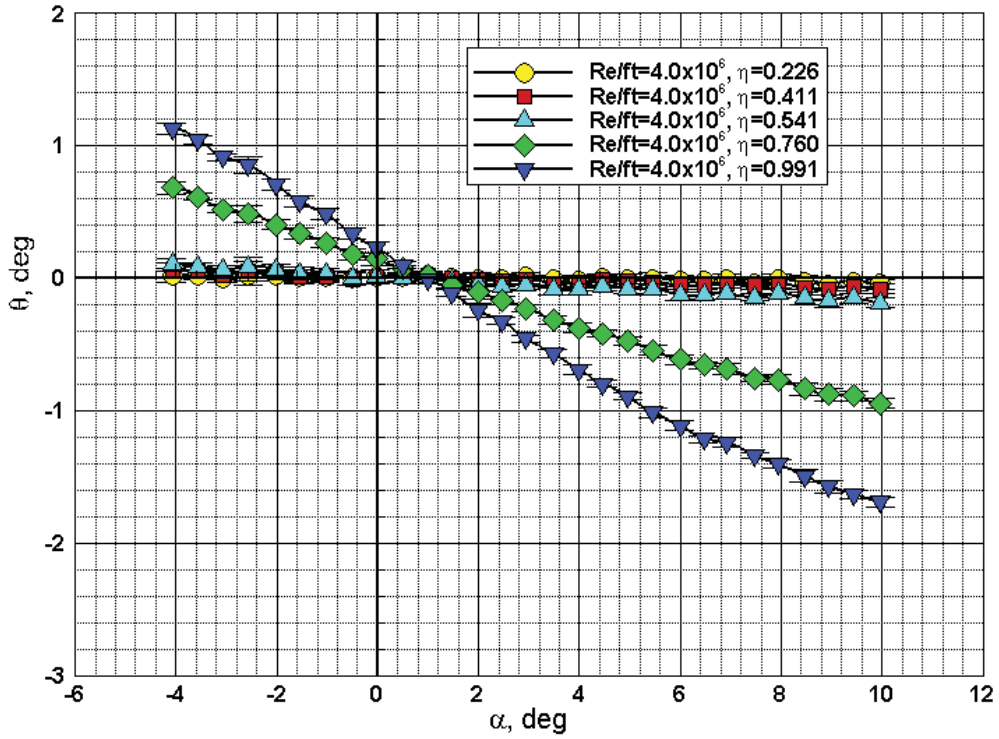

Figure 35. Variation of wing twist with angle of attack at all five measurement stations and $M_\infty = 1.8$; solid wing.

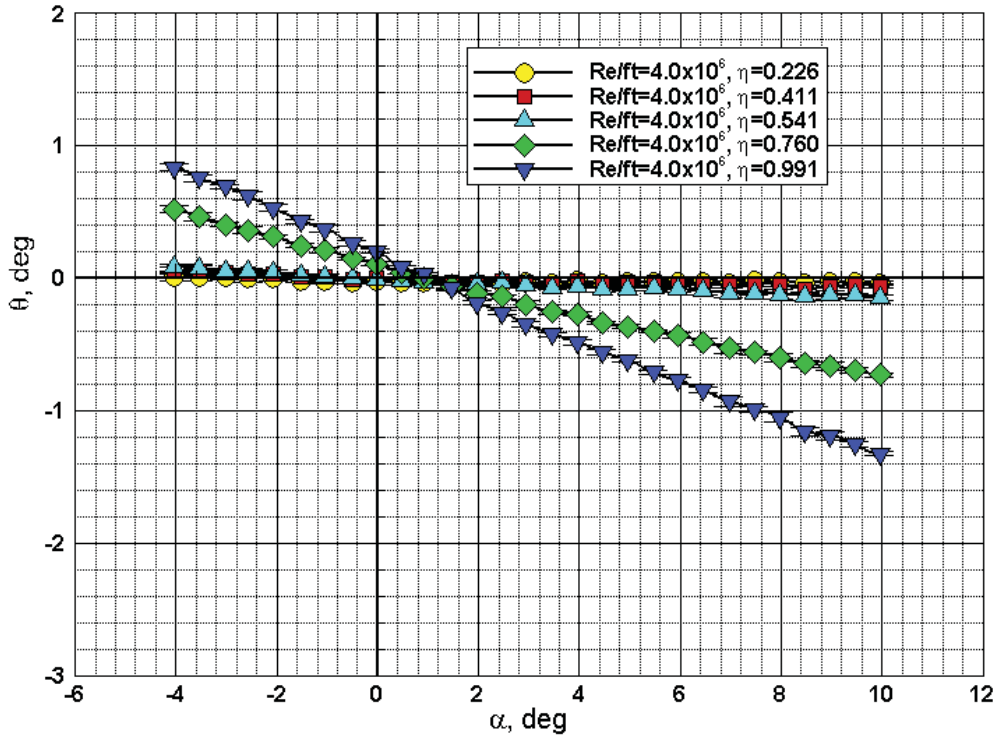

Figure 36. Variation of wing twist with angle of attack at all five measurement stations and $M_\infty = 2.1$; solid wing.

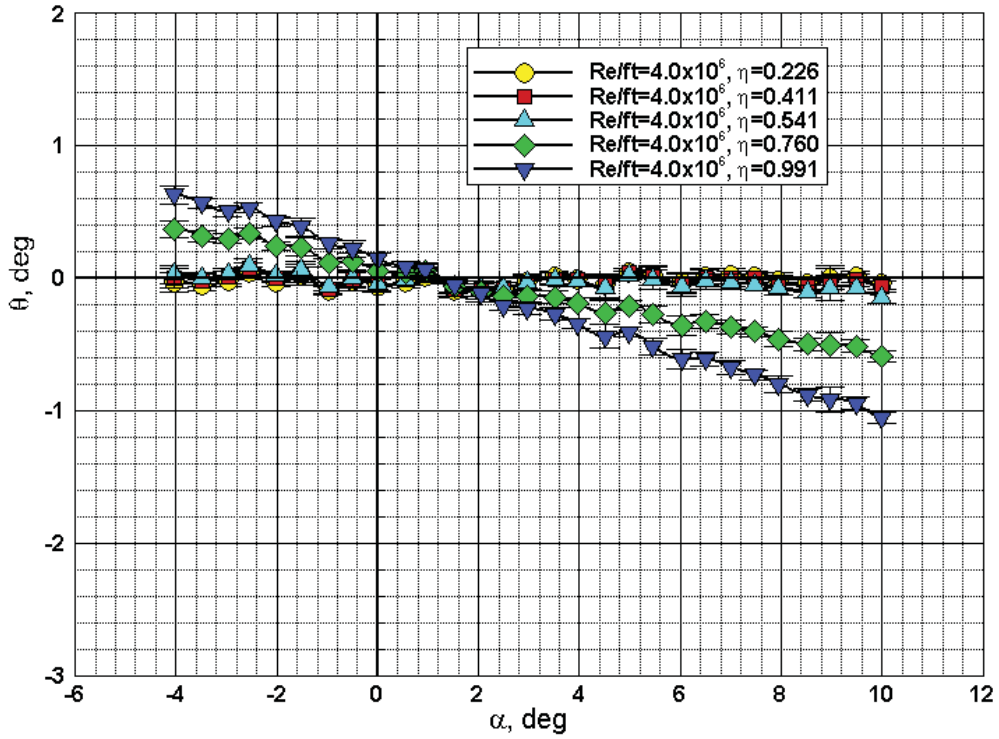

Figure 37. Variation of wing twist with angle of attack at all five measurement stations and $M_\infty = 2.4$; solid wing.

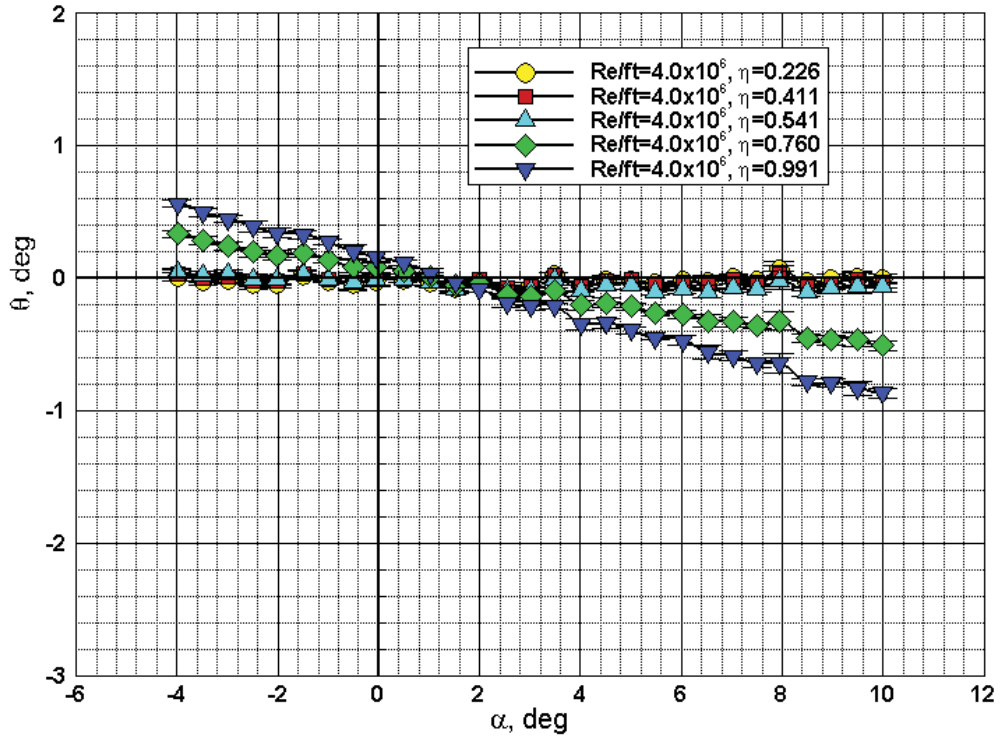

Figure 38. Variation of wing twist with angle of attack at all five measurement stations and $M_\infty = 2.7$; solid wing.

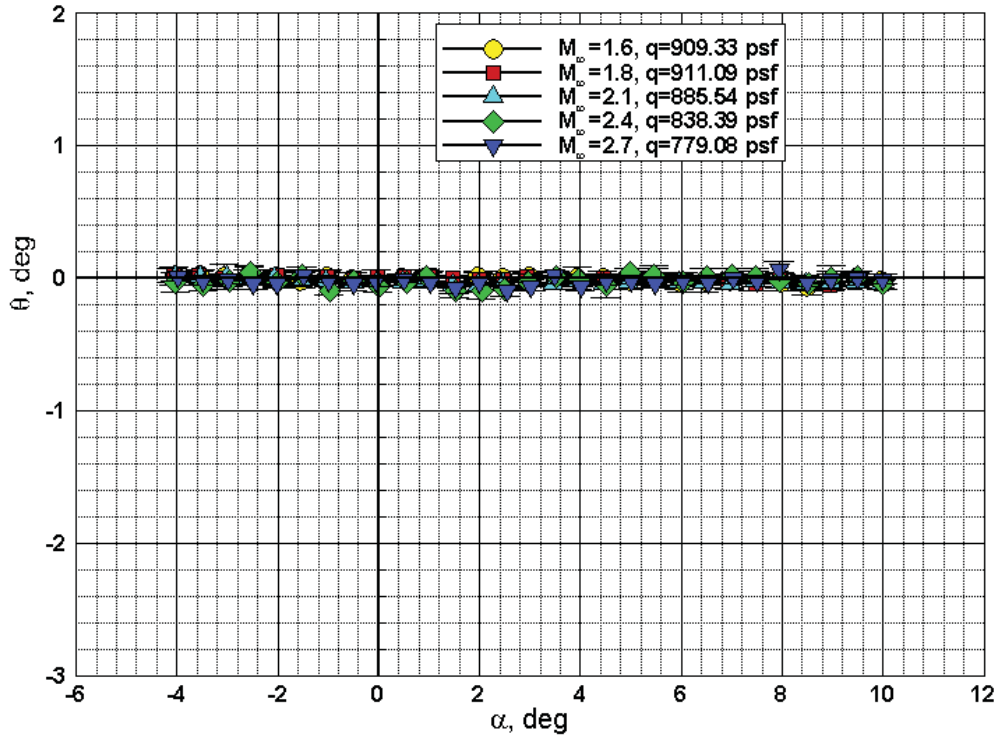

Figure 39. Effect of Mach number on wing twist at Re/ft = 4.0 x10^6 and $\eta = 0.226$; solid wing.

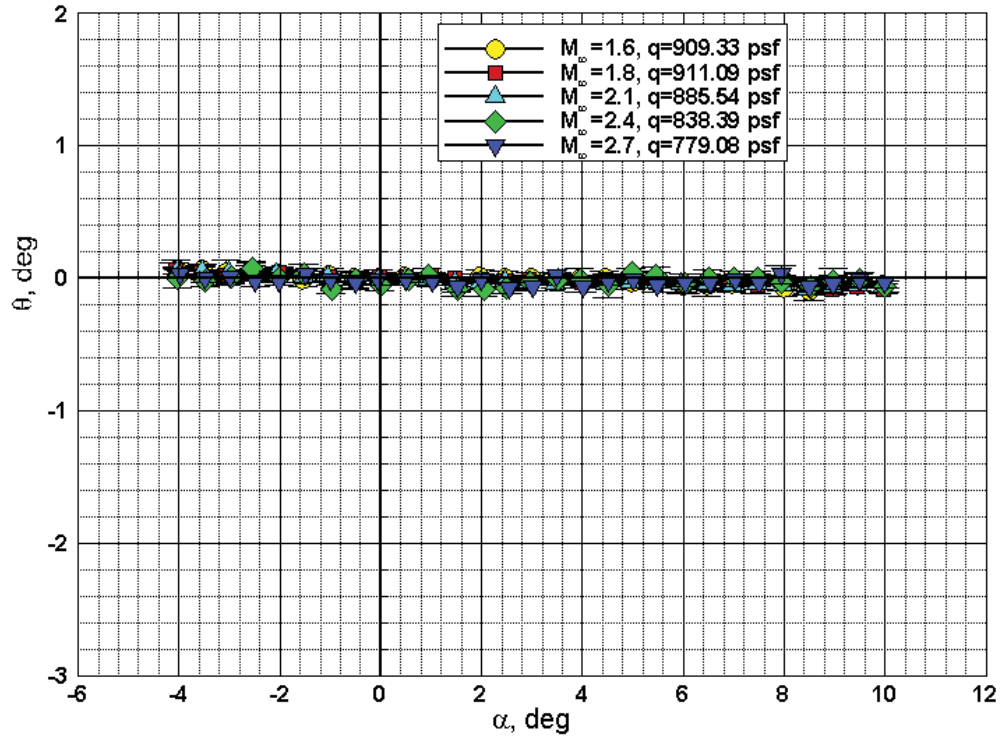

Figure 40. Effect of Mach number on wing twist at Re/ft = 4.0 x10^6 and η = 0.411; solid wing.

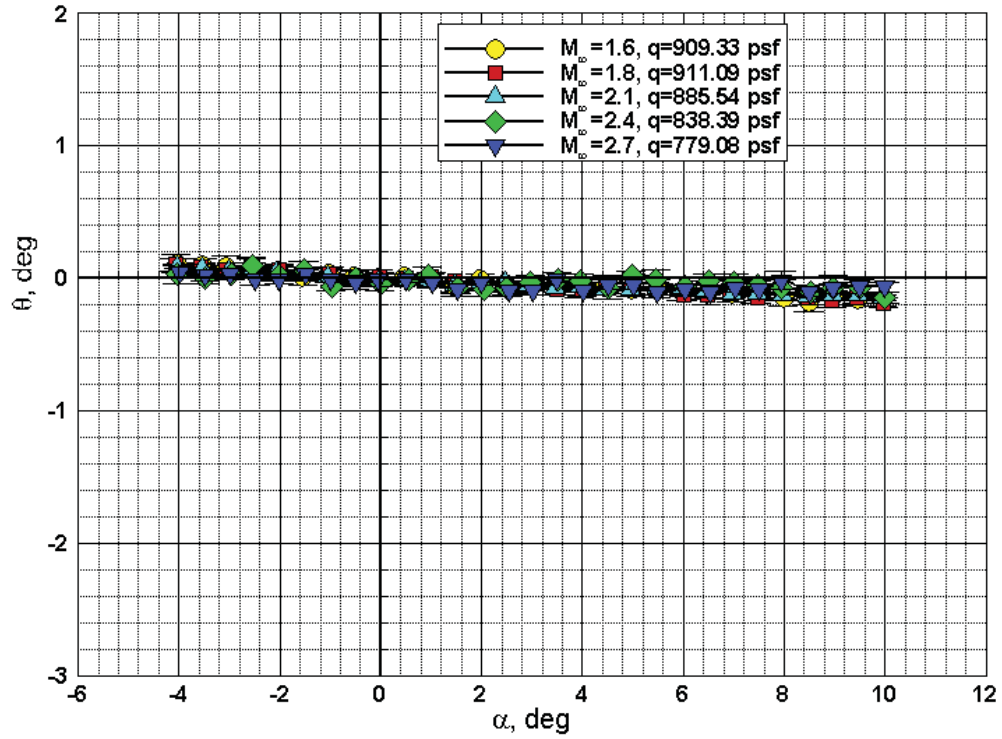

Figure 41. Effect of Mach number on wing twist at Re/ft = 4.0 x10^6 and η = 0.541; solid wing.

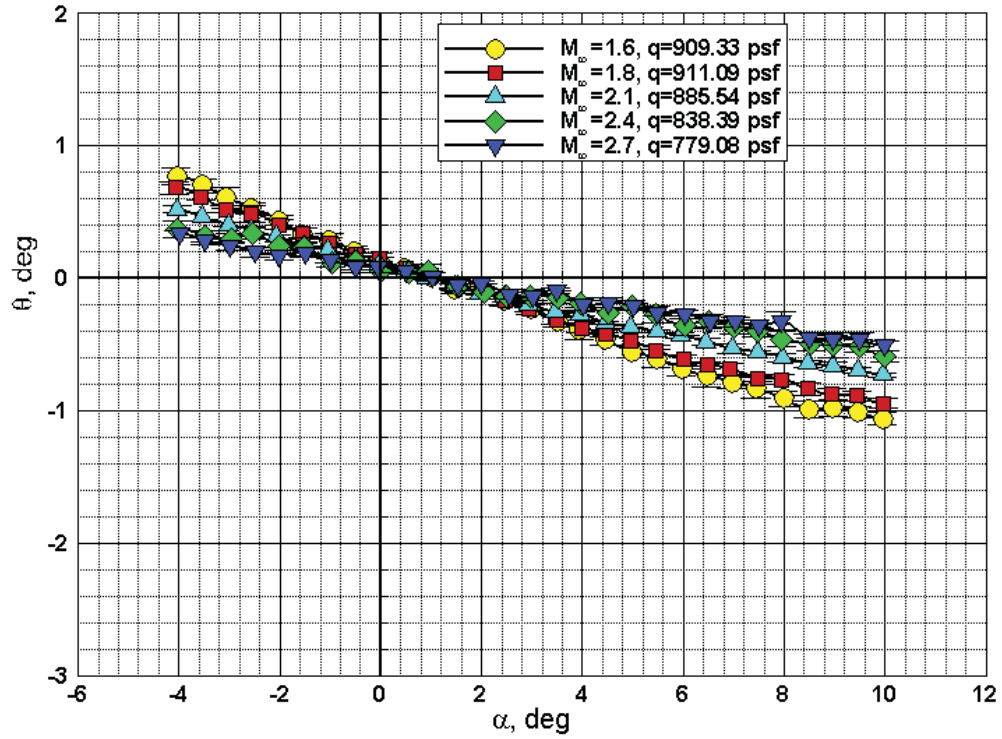

Figure 42. Effect of Mach number on wing twist at Re/ft = 4.0 x10^6 and η = 0.760; solid wing.

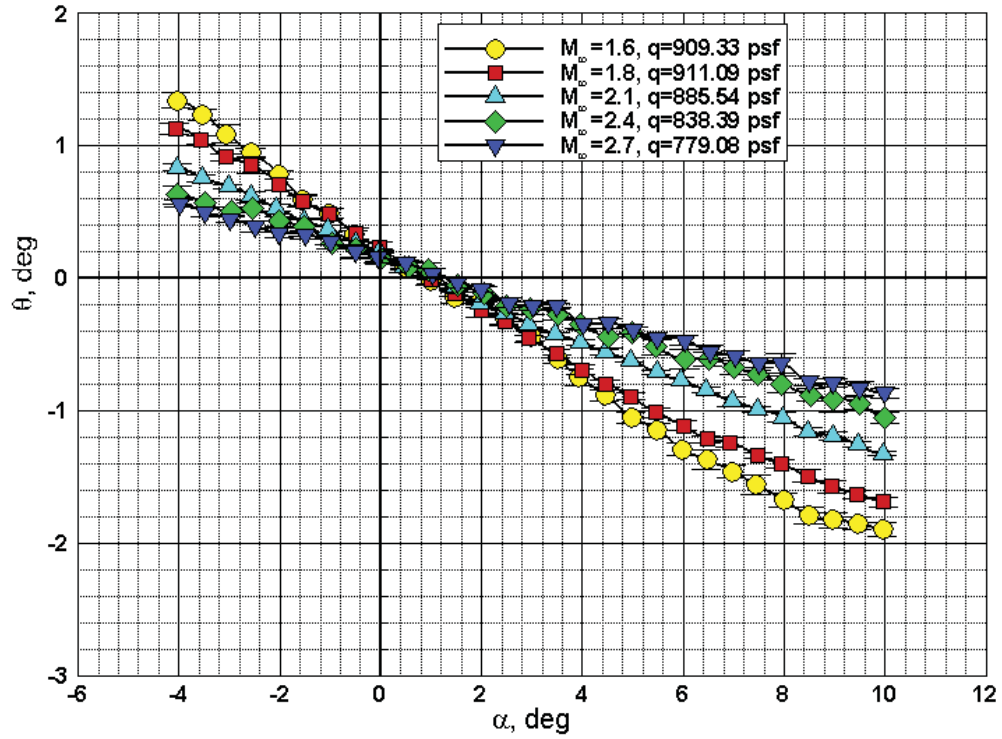

Figure 43. Effect of Mach number on wing twist at Re/ft = 4.0 x10^6 and η = 0.991; solid wing.

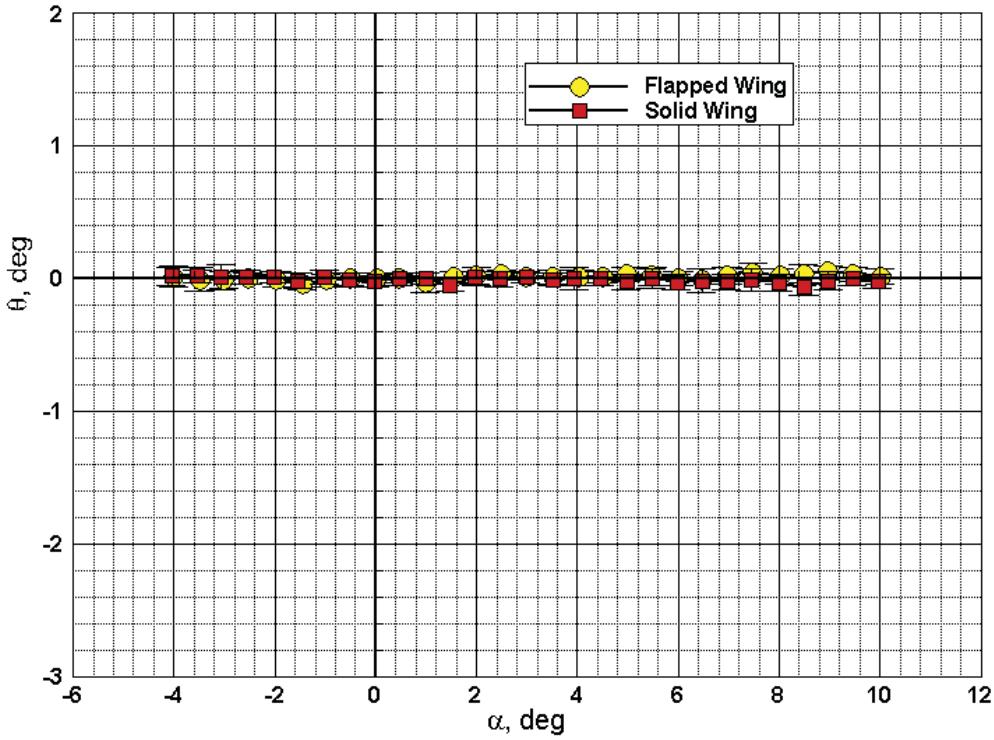

(a) $\eta = 0.226$

Figure 44. Comparison of flapped wing and solid wing twist at $M_\infty = 1.6$ and Re/ft = 4.0 x10^6.

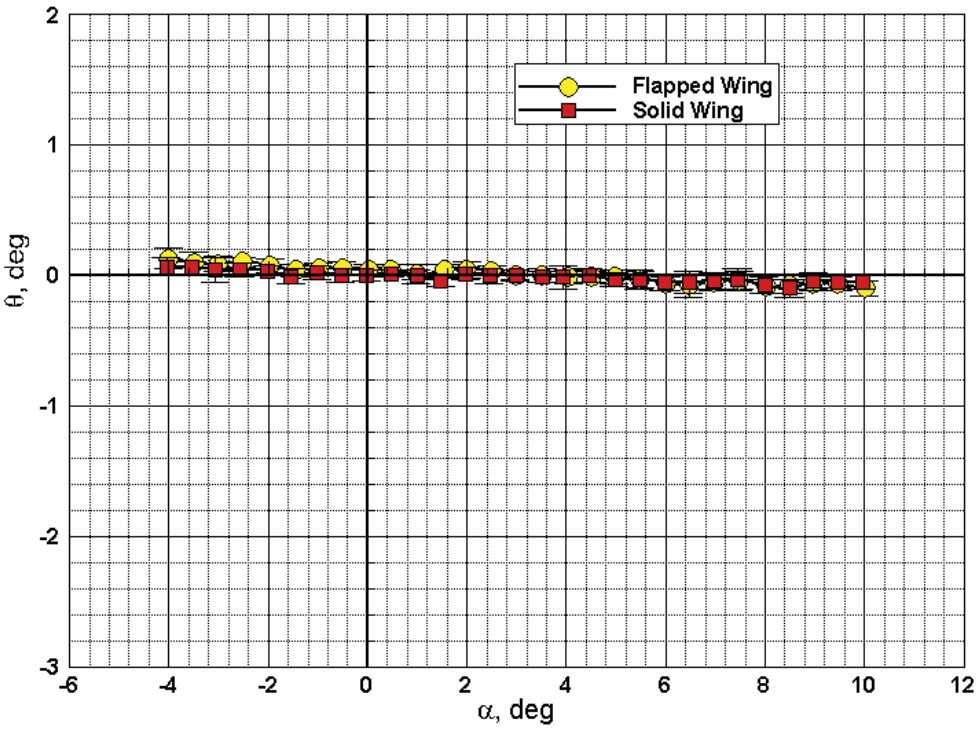

(b) $\eta = 0.411$

Figure 44. Comparison of flapped wing and solid wing twist at $M_\infty = 1.6$ and Re/ft = 4.0 x10^6.

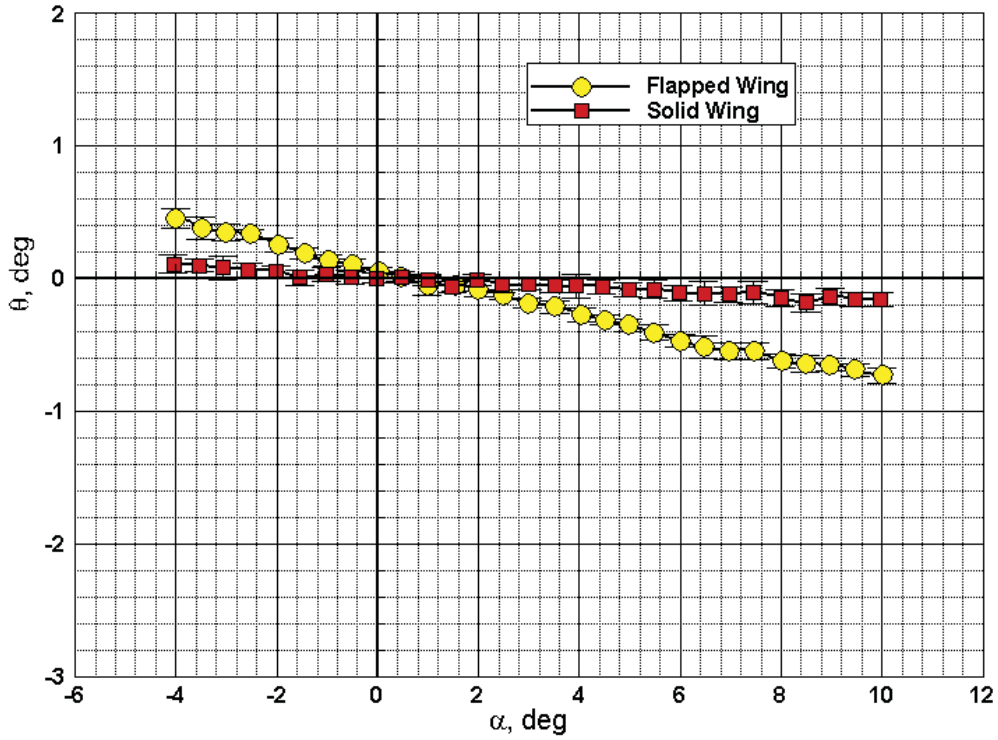

(c) $\eta = 0.541$

Figure 44. Comparison of flapped wing and solid wing twist at $M_\infty = 1.6$ and Re/ft = 4.0 x10^6.

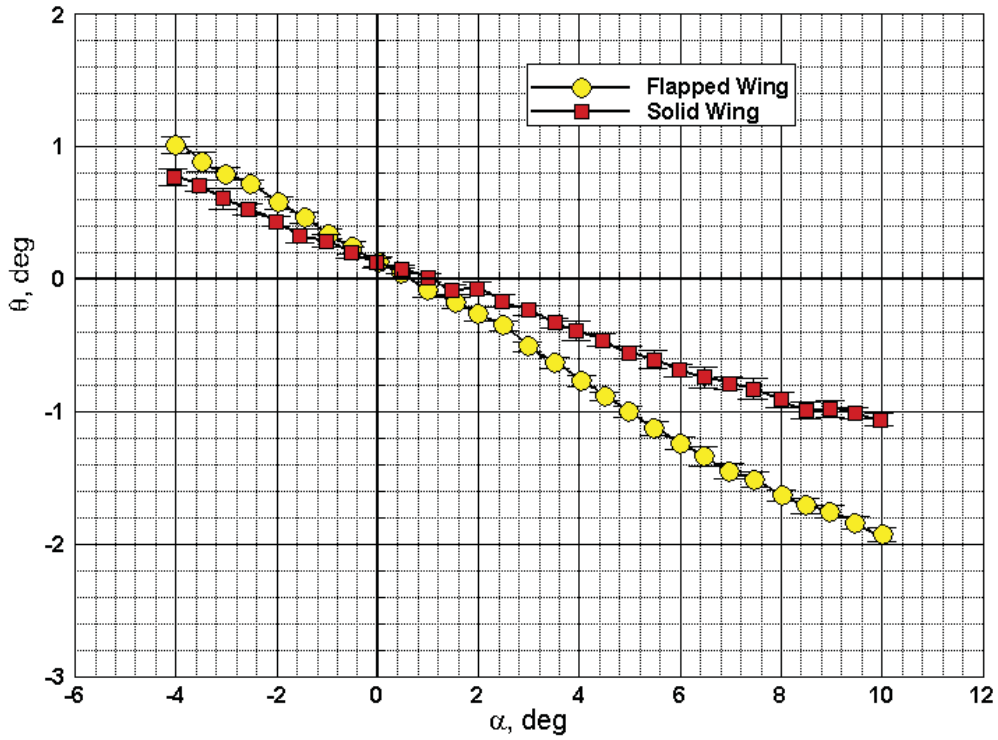

(d) $\eta = 0.760$

Figure 44. Comparison of flapped wing and solid wing twist at $M_\infty = 1.6$ and Re/ft = 4.0 x10^6.

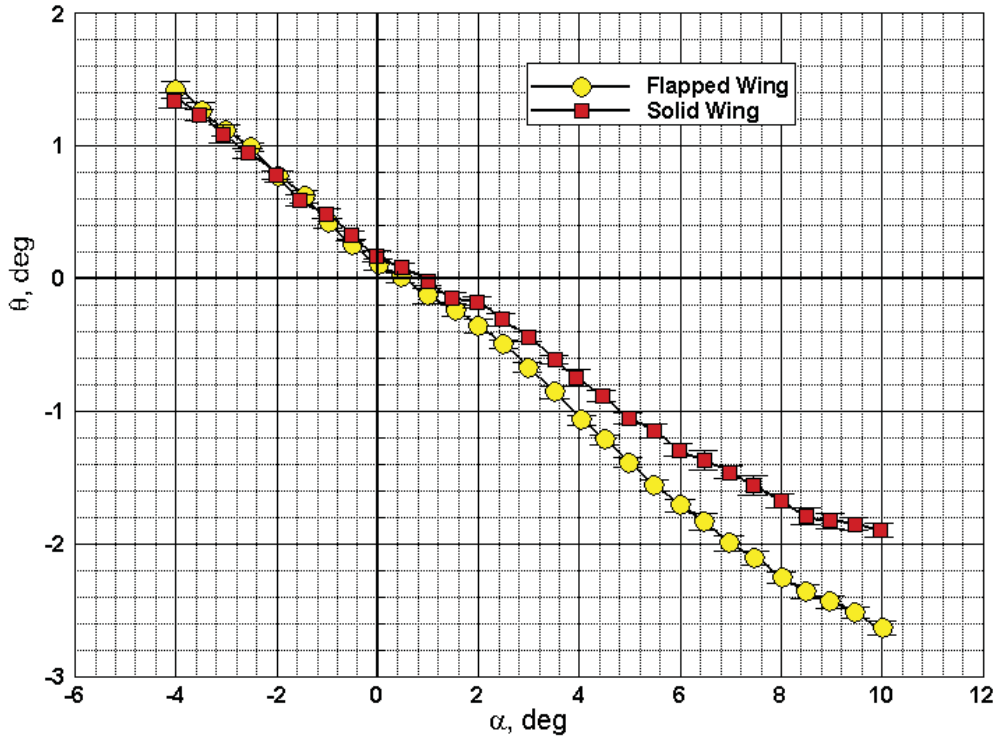

(e) $\eta = 0.991$

Figure 44. Comparison of flapped wing and solid wing twist at $M_\infty = 1.6$ and Re/ft = 4.0 x10^6.

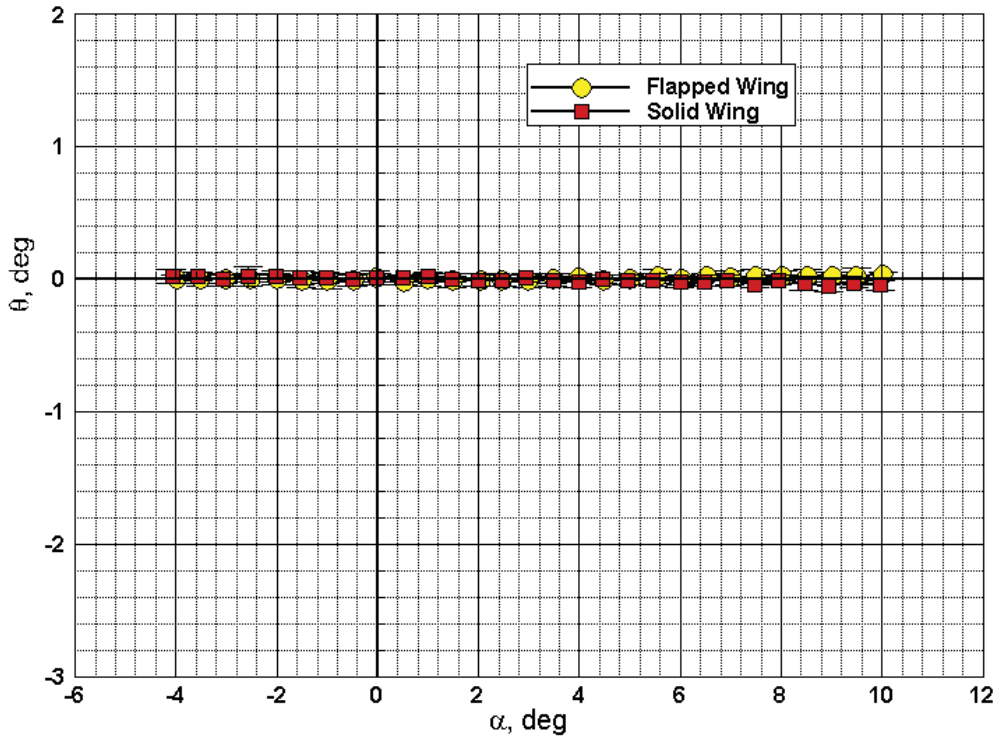

(a) $\eta = 0.226$

Figure 45. Comparison of flapped wing and solid wing twist at $M_\infty = 1.8$ and Re/ft = 4.0 x10^6.

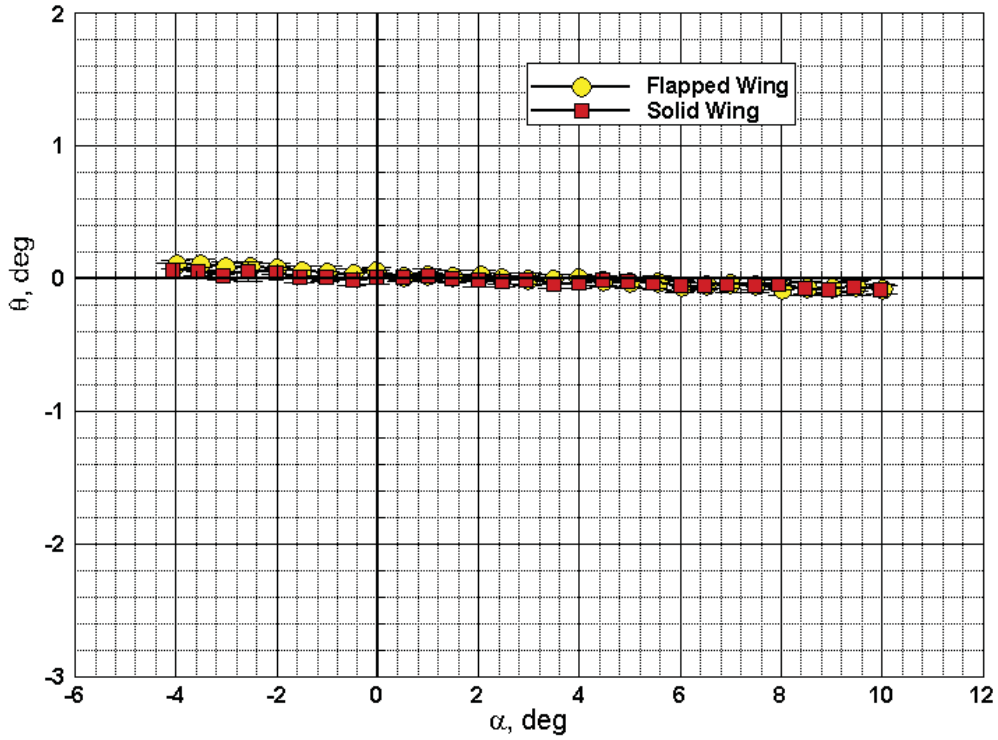

(b) $\eta = 0.411$

Figure 45. Comparison of flapped wing and solid wing twist at $M_\infty = 1.8$ and Re/ft = 4.0 x10^6.

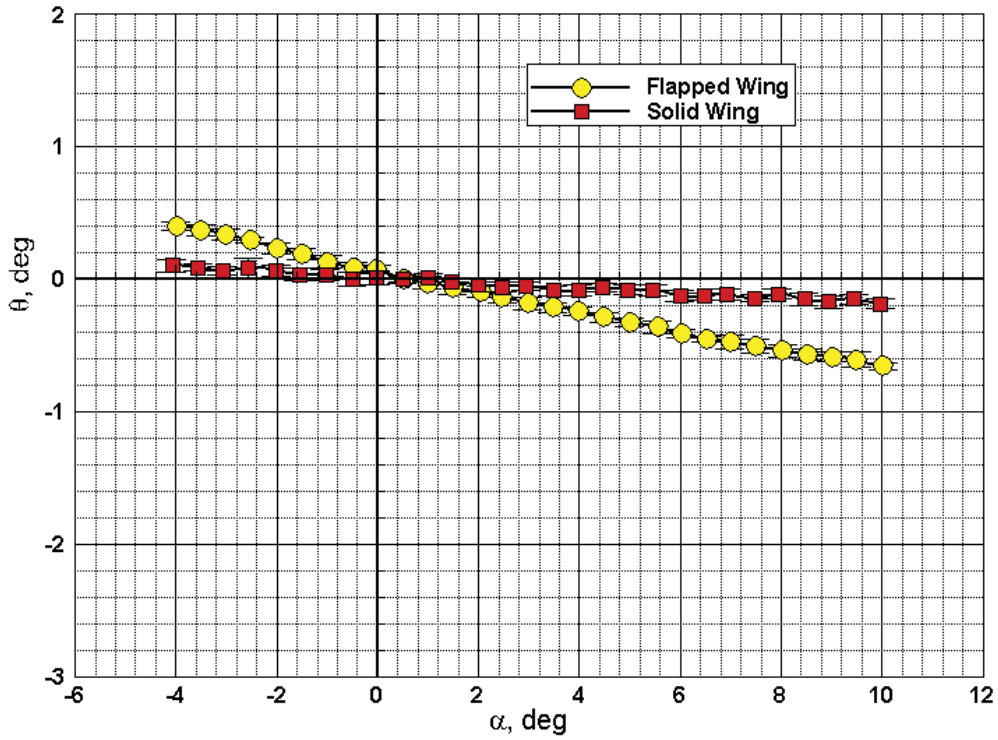

(c) $\eta = 0.541$

Figure 45. Comparison of flapped wing and solid wing twist at $M_\infty = 1.8$ and Re/ft = 4.0 x10^6.

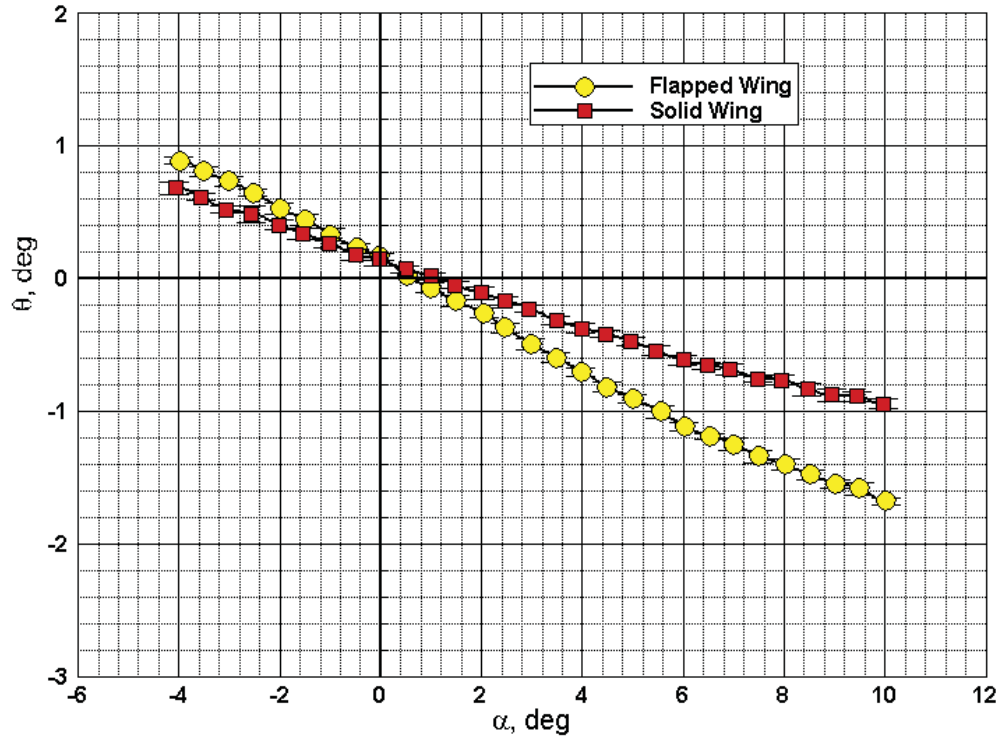

(d) $\eta = 0.760$

Figure 45. Comparison of flapped wing and solid wing twist at $M_\infty = 1.8$ and Re/ft = 4.0 x10^6.

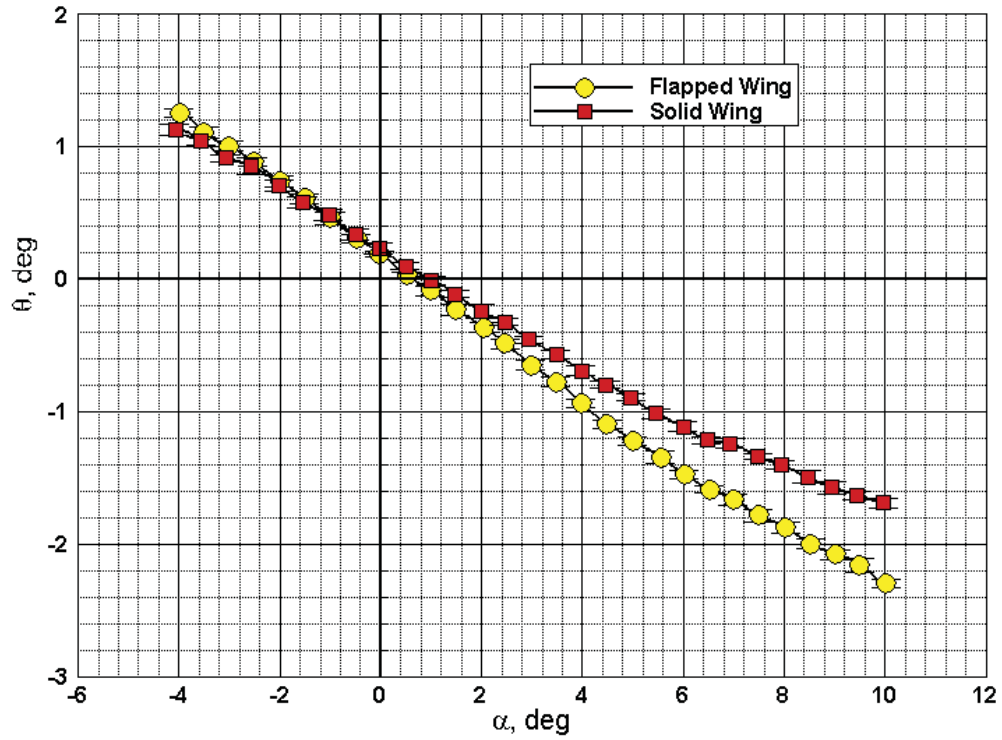

(e) $\eta = 0.991$

Figure 45. Comparison of flapped wing and solid wing twist at $M_\infty = 1.8$ and Re/ft = 4.0 x 10^6.

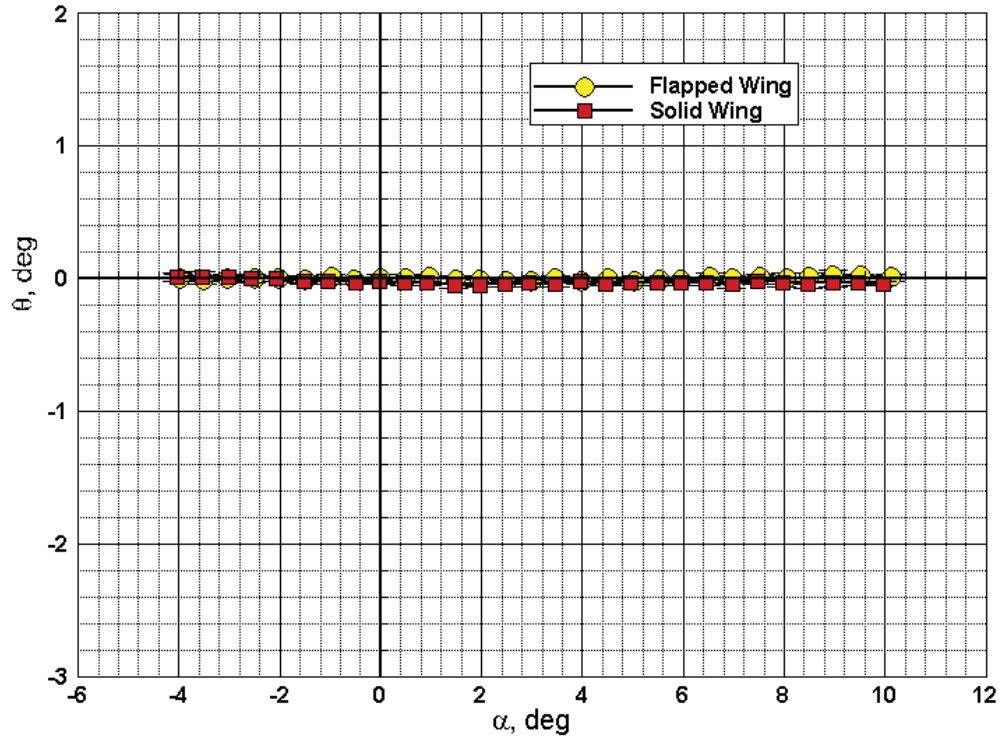

(a) $\eta = 0.226$

Figure 46. Comparison of flapped wing and solid wing twist at $M_\infty = 2.1$ and Re/ft = 4.0 x 10^6.

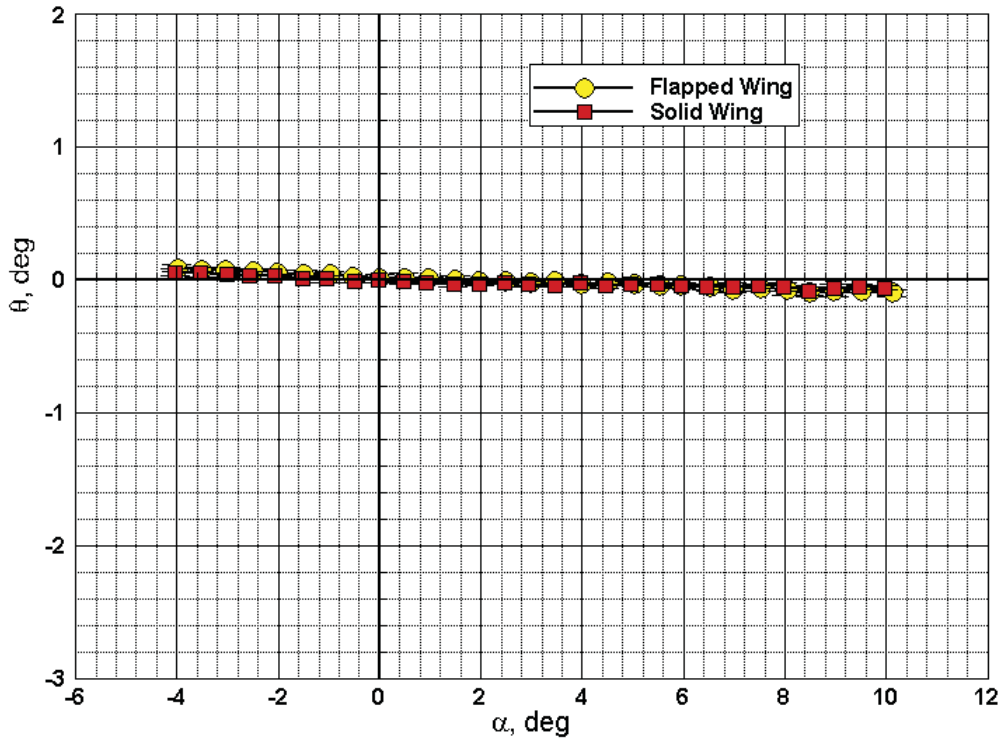

(b) $\eta = 0.411$

Figure 46. Comparison of flapped wing and solid wing twist at $M_\infty = 2.1$ and Re/ft = 4.0 x 10^6.

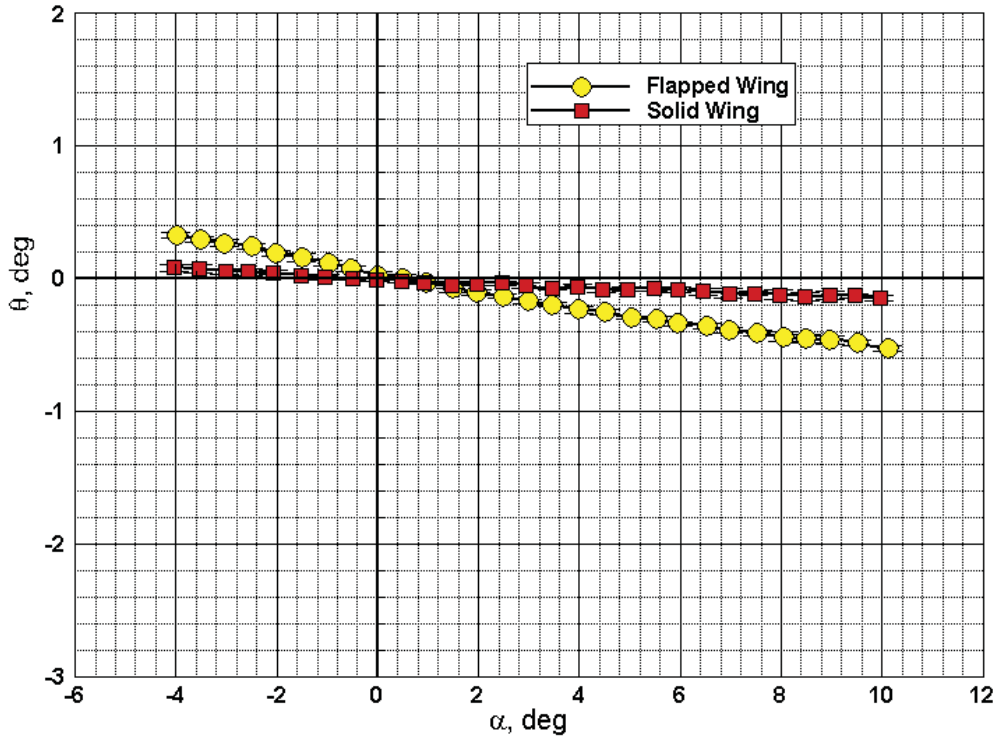

(c) $\eta = 0.541$

Figure 46. Comparison of flapped wing and solid wing twist at $M_\infty = 2.1$ and Re/ft = 4.0 x 10^6.

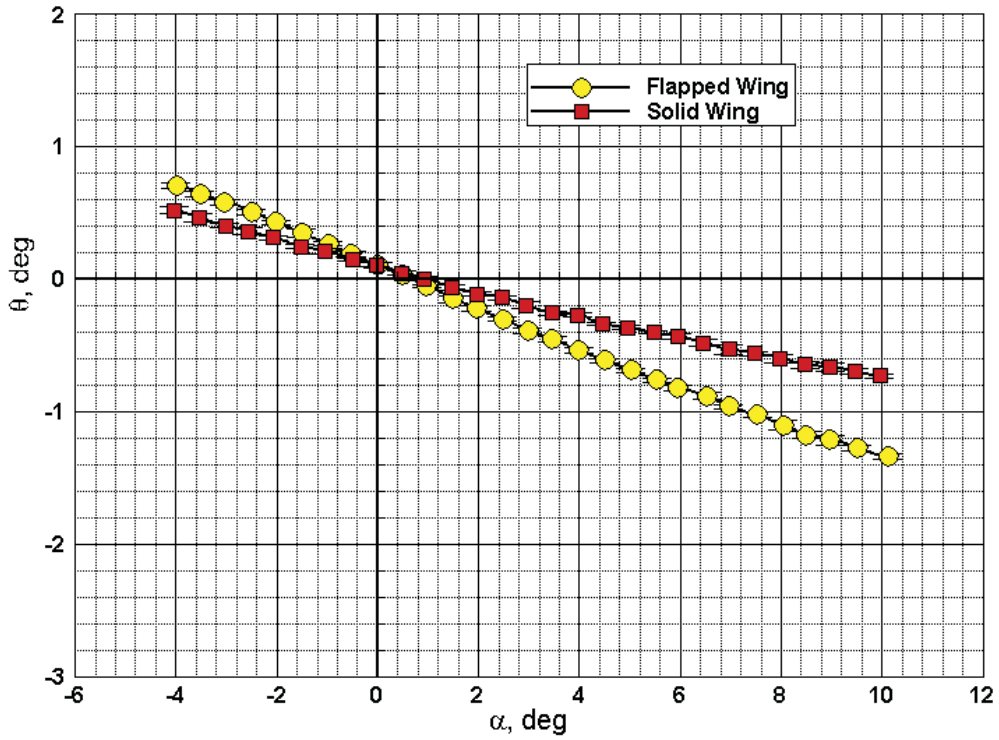

(d) $\eta = 0.760$

Figure 46. Comparison of flapped wing and solid wing twist at $M_\infty = 2.1$ and Re/ft = 4.0 x 10^6.

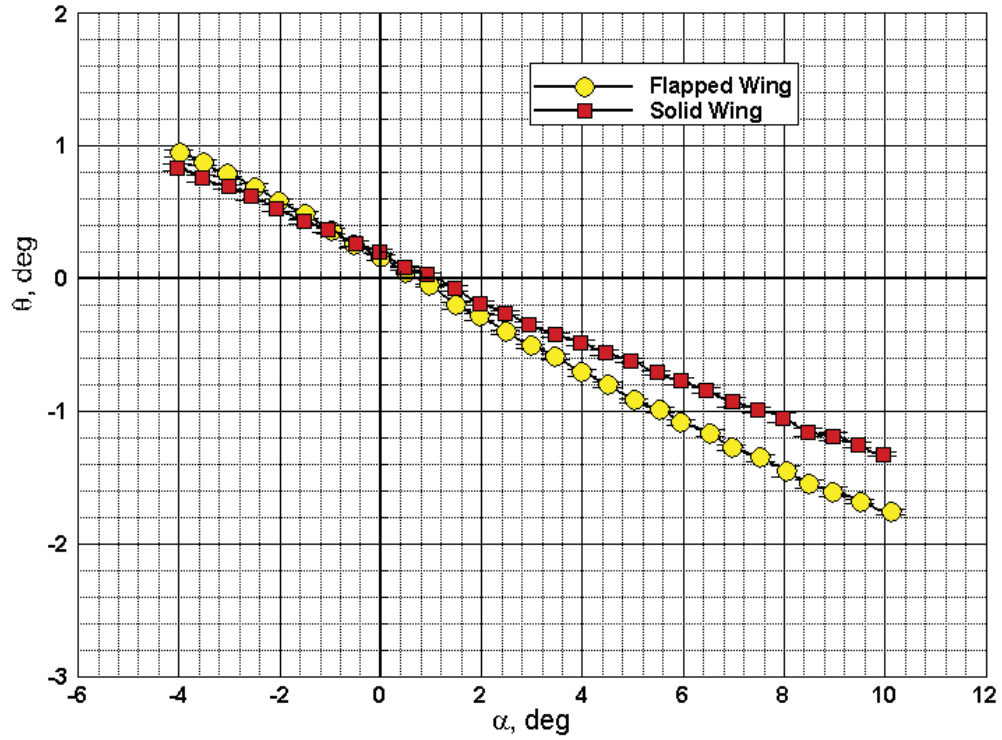

(e) $\eta = 0.991$

Figure 46. Comparison of flapped wing and solid wing twist at $M_\infty = 2.1$ and Re/ft = 4.0 x 10^6.

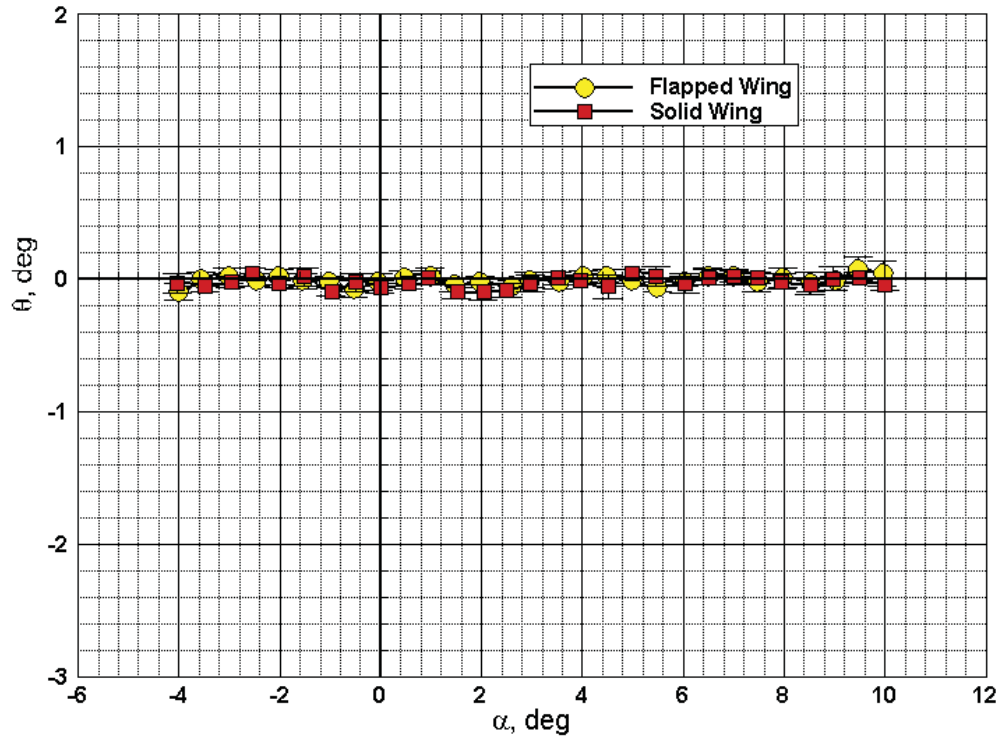

(a) $\eta = 0.226$

Figure 47. Comparison of flapped wing and solid wing twist at $M_\infty = 2.4$ and Re/ft = 4.0 x 10^6.

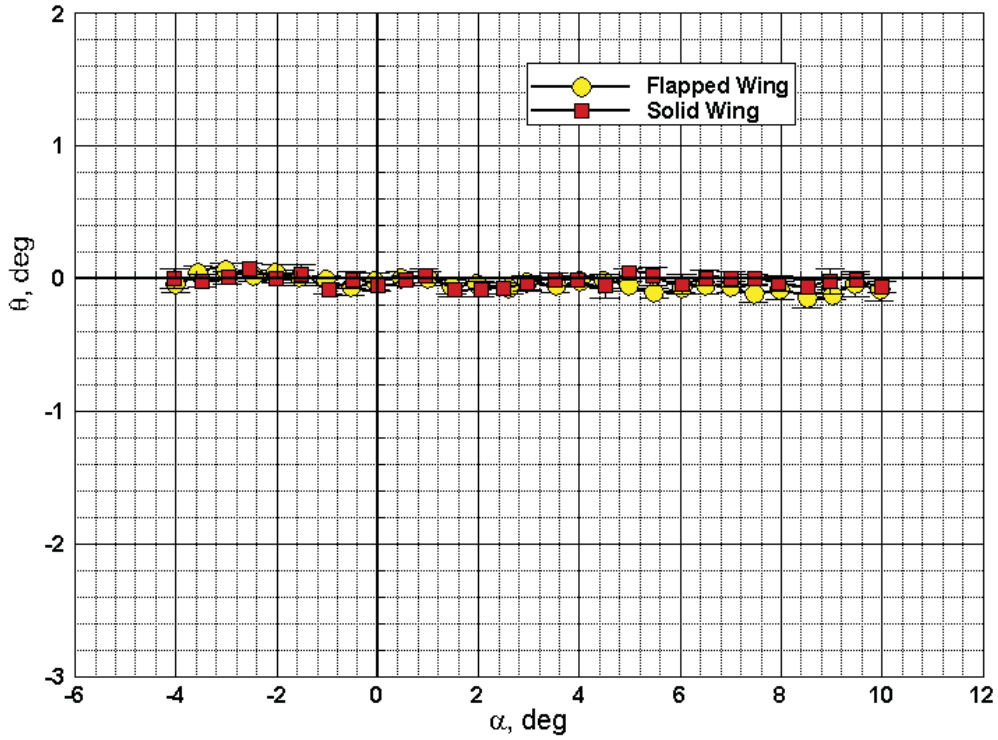

(b) $\eta = 0.411$

Figure 47. Comparison of flapped wing and solid wing twist at $M_\infty = 2.4$ and Re/ft = 4.0 x 10^6.

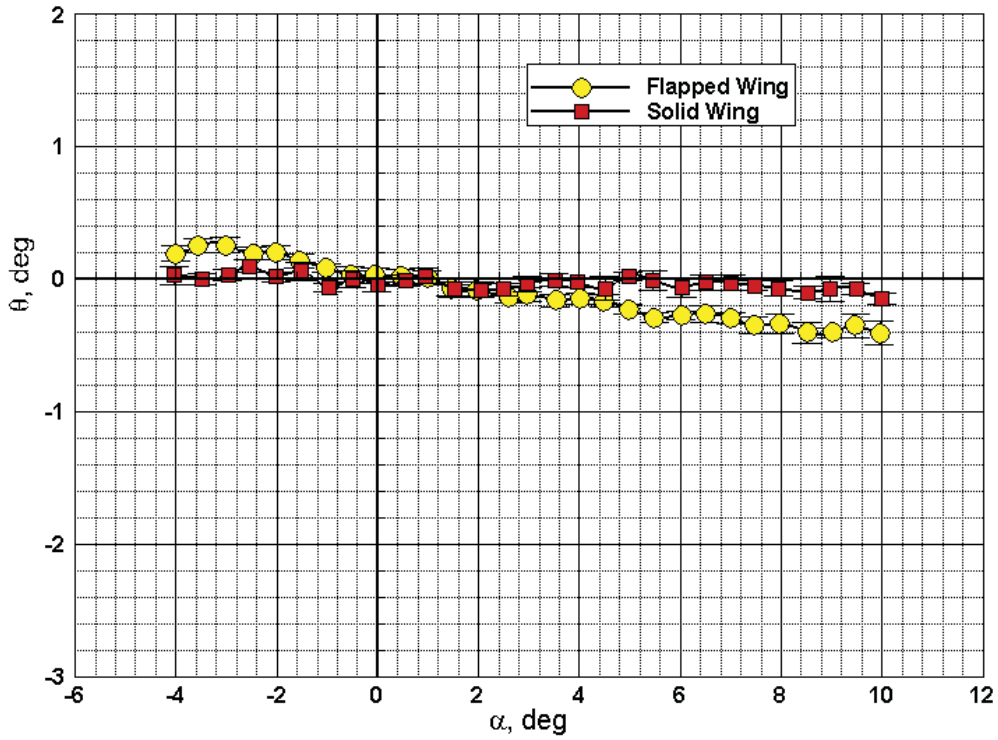

(c) $\eta = 0.541$

Figure 47. Comparison of flapped wing and solid wing twist at $M_\infty = 2.4$ and Re/ft = 4.0 x 10^6.

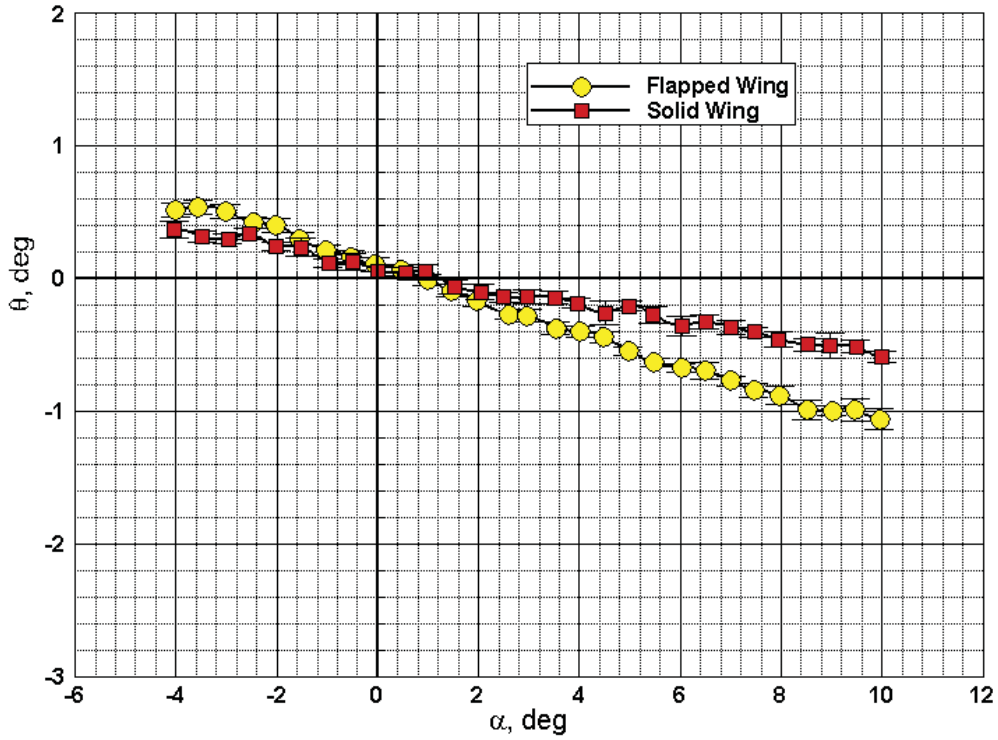

(d) $\eta = 0.760$

Figure 47. Comparison of flapped wing and solid wing twist at $M_\infty = 2.4$ and Re/ft = 4.0 x 10^6.

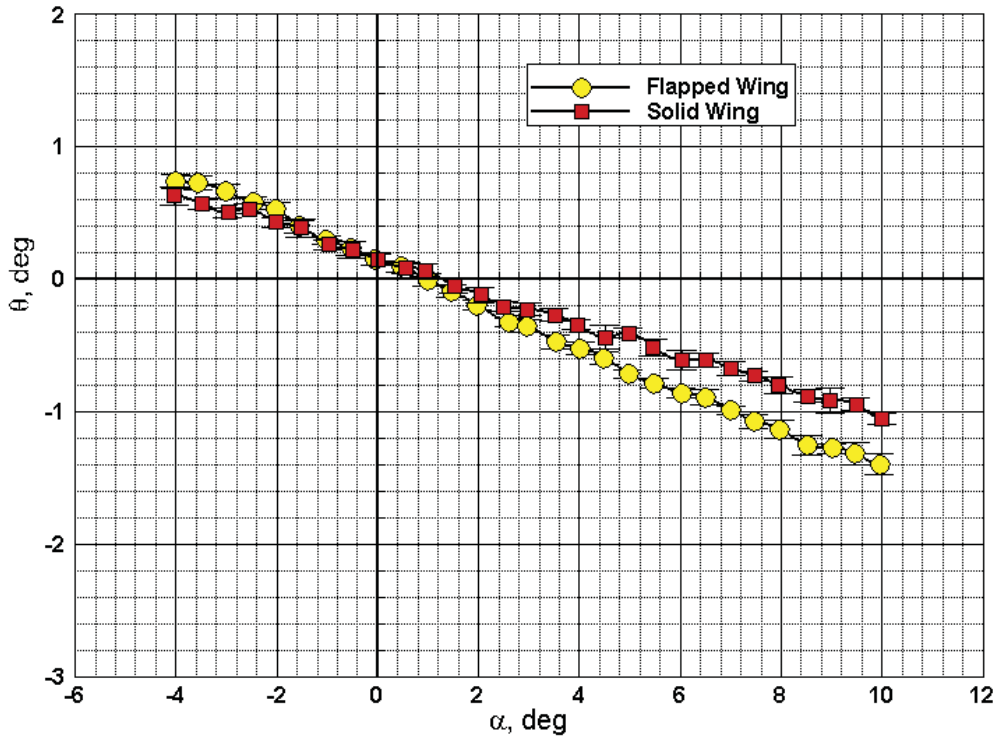

(e) $\eta = 0.991$

Figure 47. Comparison of flapped wing and solid wing twist at $M_\infty = 2.4$ and Re/ft = 4.0 x 10^6.

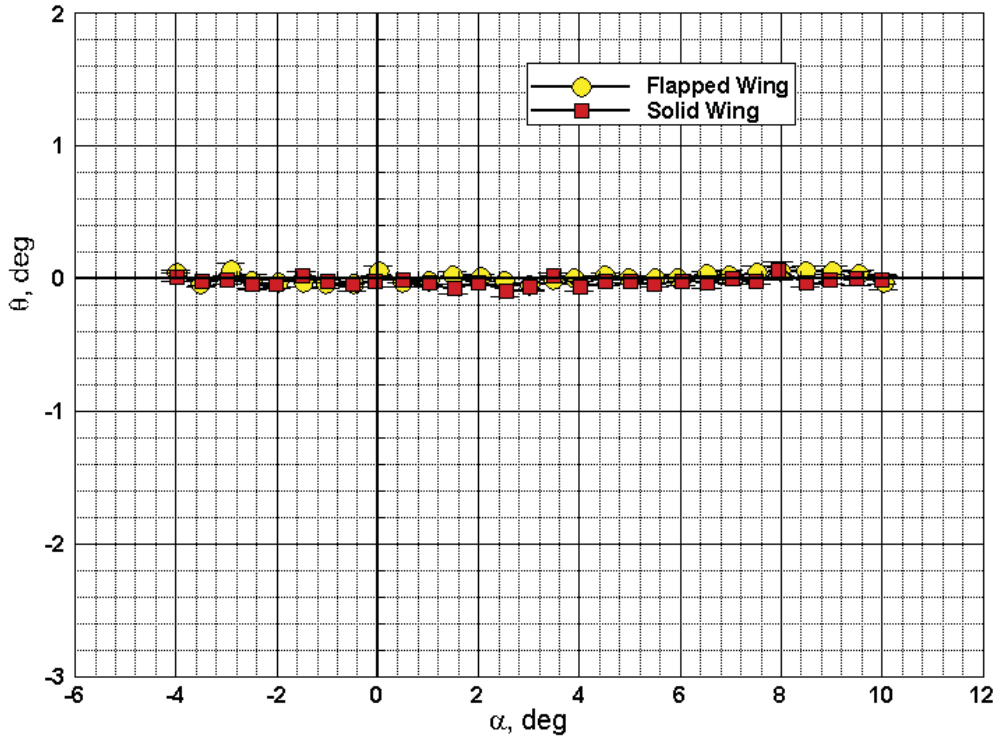

(a) $\eta = 0.226$

Figure 48. Comparison of flapped wing and solid wing twist at $M_\infty = 2.7$ and Re/ft = 4.0 x 10^6.

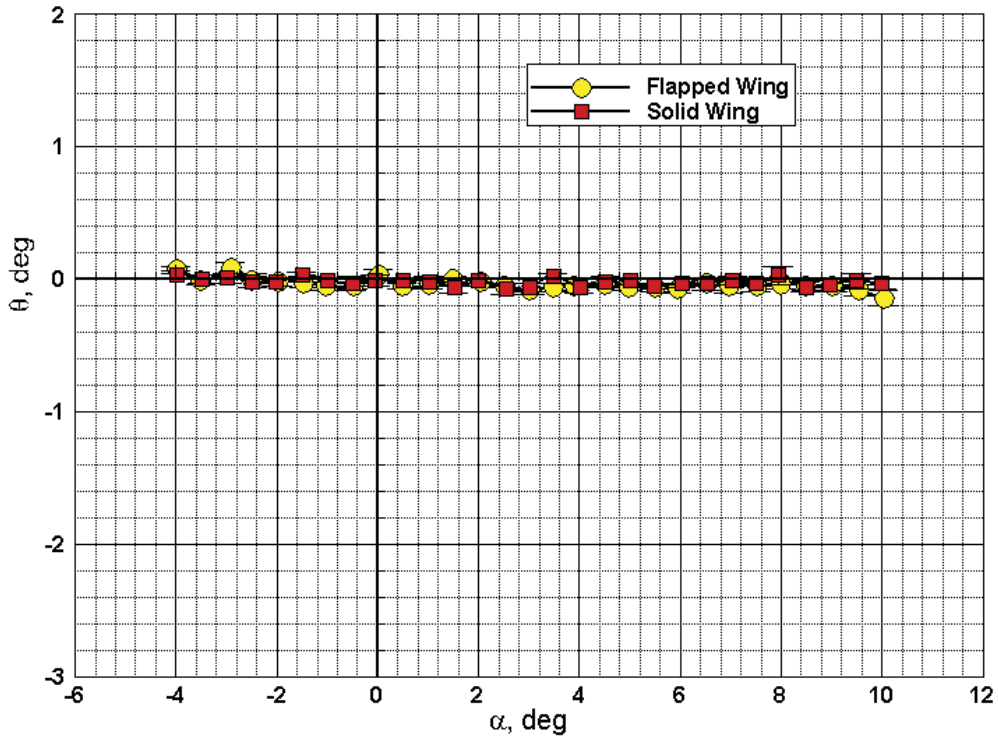

(b) $\eta = 0.411$

Figure 48. Comparison of flapped wing and solid wing twist at $M_\infty = 2.7$ and Re/ft = 4.0 x 10^6.

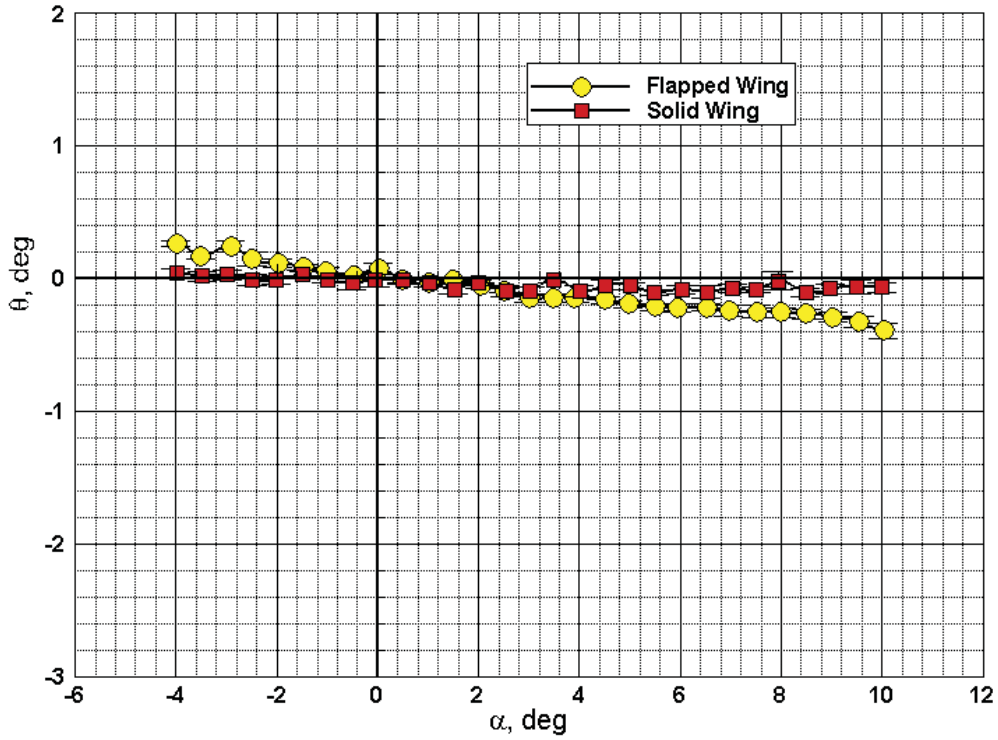

(c) $\eta = 0.541$

Figure 48. Comparison of flapped wing and solid wing twist at $M_\infty = 2.7$ and Re/ft = 4.0 x 10^6.

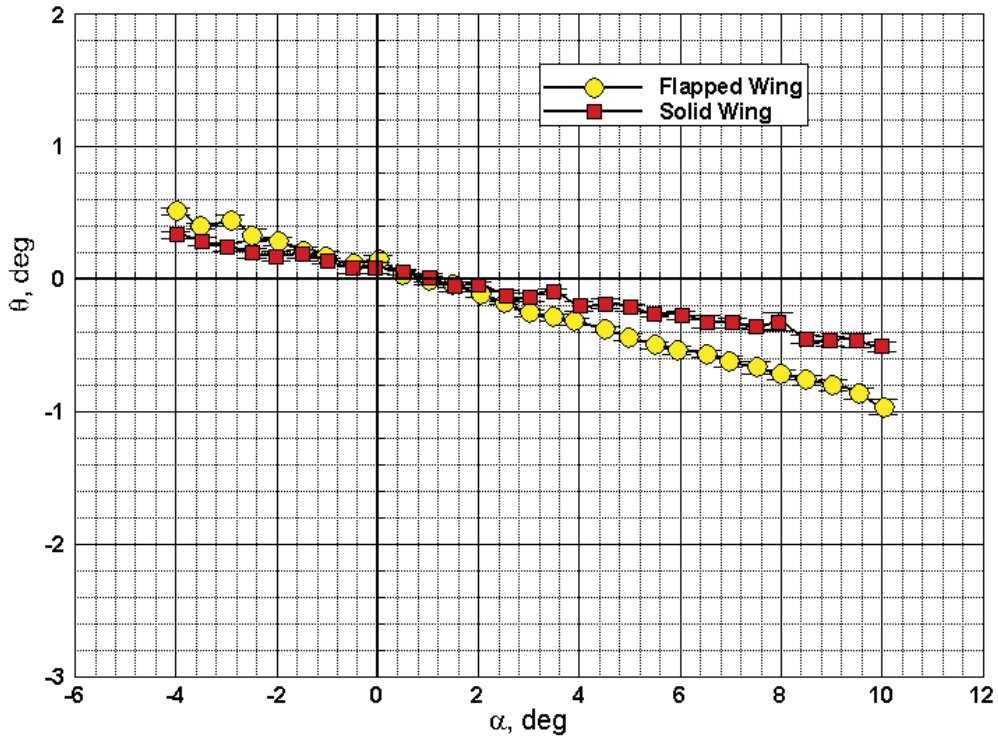

(d) $\eta = 0.760$

Figure 48. Comparison of flapped wing and solid wing twist at $M_\infty = 2.7$ and Re/ft = 4.0 x 10^6.

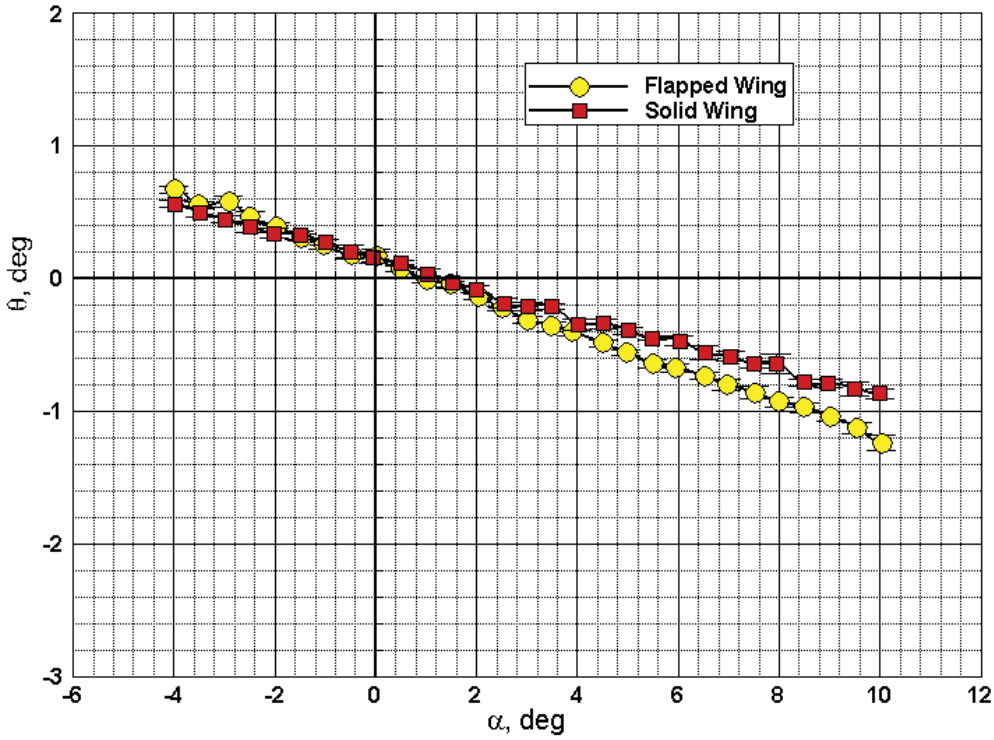

(e) $\eta = 0.991$

Figure 48. Comparison of flapped wing and solid wing twist at $M_\infty = 2.7$ and Re/ft = 4.0 x 10^6.

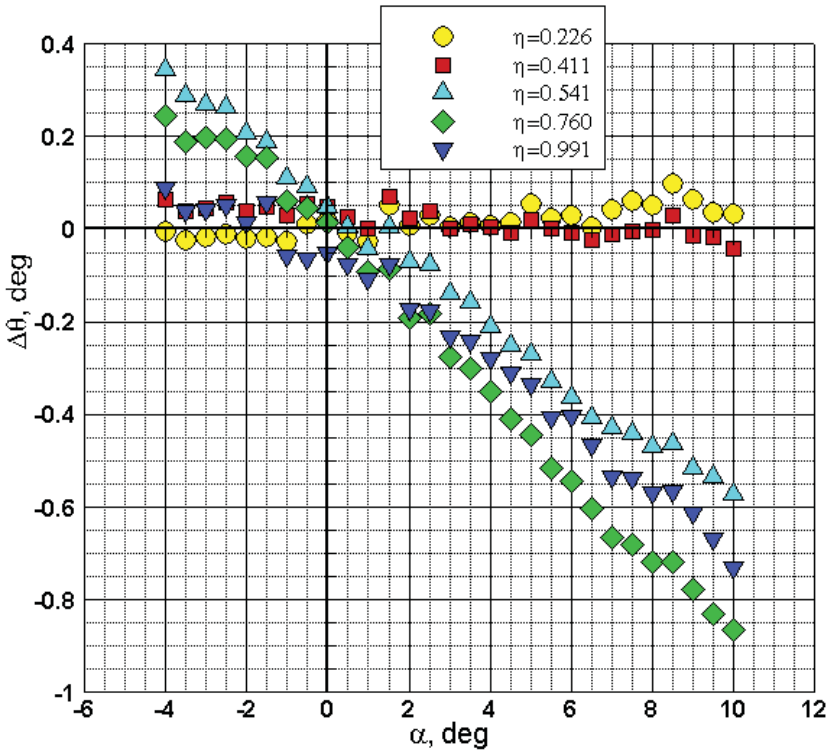

Figure 49. Differences between flapped wing and solid wing twist angles at all five measurement stations; $M_\infty = 1.6$, Re/ft = 4.0 x 10^6.

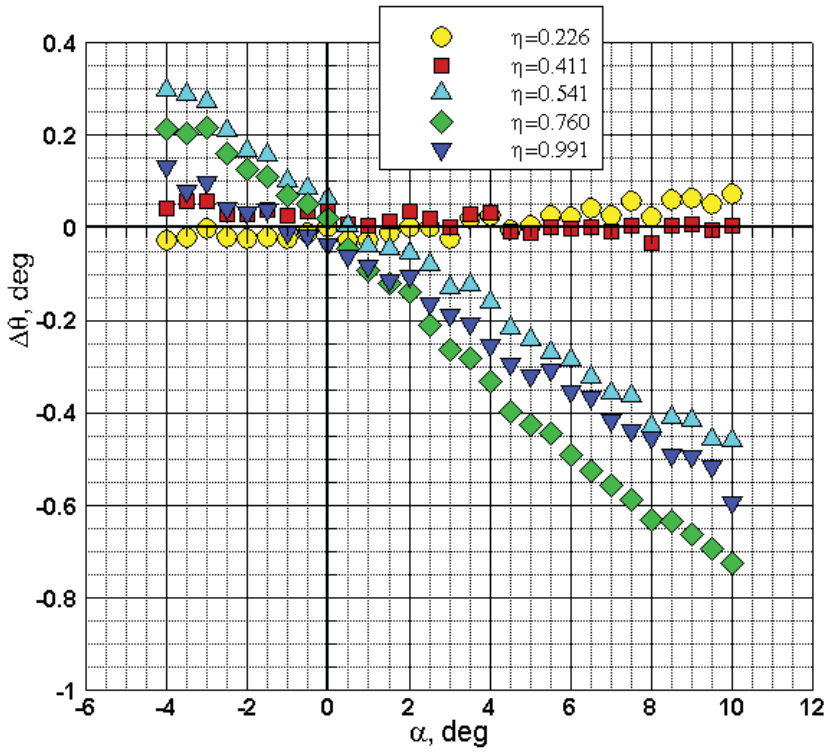

Figure 50. Differences between flapped wing and solid wing twist angles at all five measurement stations; $M_\infty = 1.8$, Re/ft = 4.0 x 10^6.

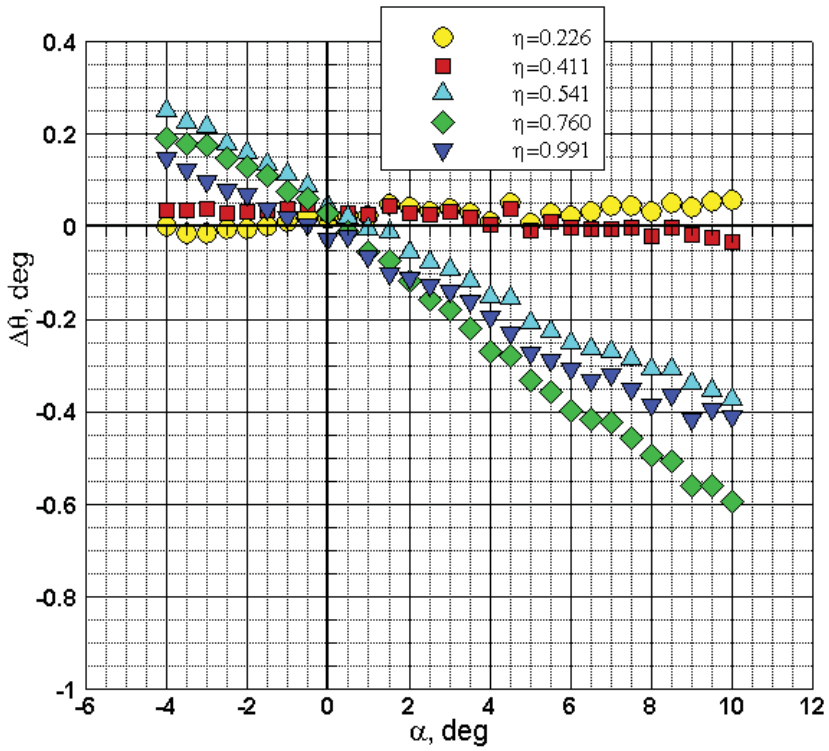

Figure 51. Differences between flapped wing and solid wing twist angles at all five measurement stations; $M_\infty = 2.1$, Re/ft = 4.0 x 10^6.

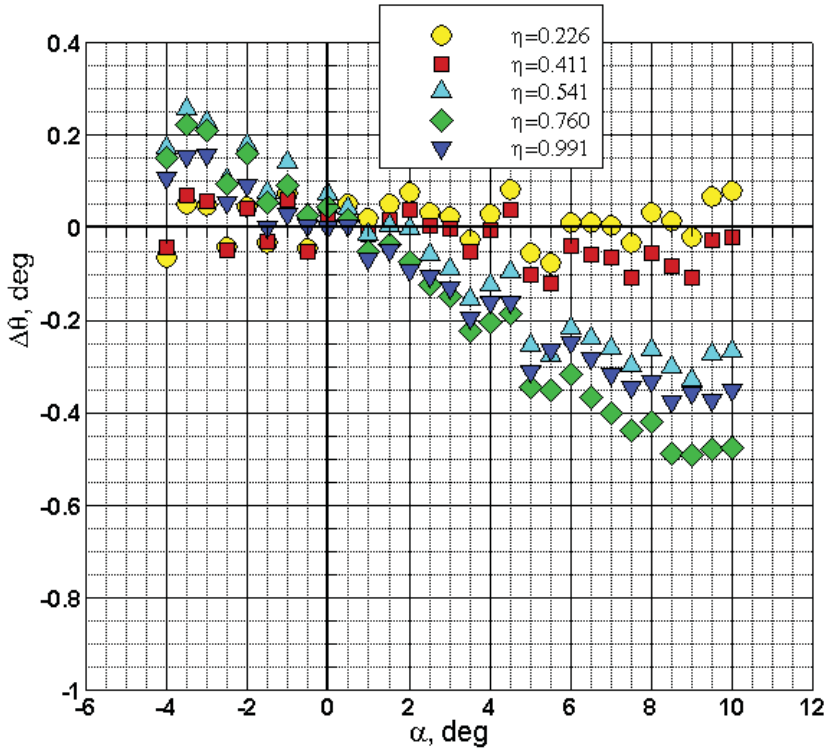

Figure 52. Differences between flapped wing and solid wing twist angles at all five measurement stations; $M_\infty = 2.4$, Re/ft = 4.0 x 10^6.

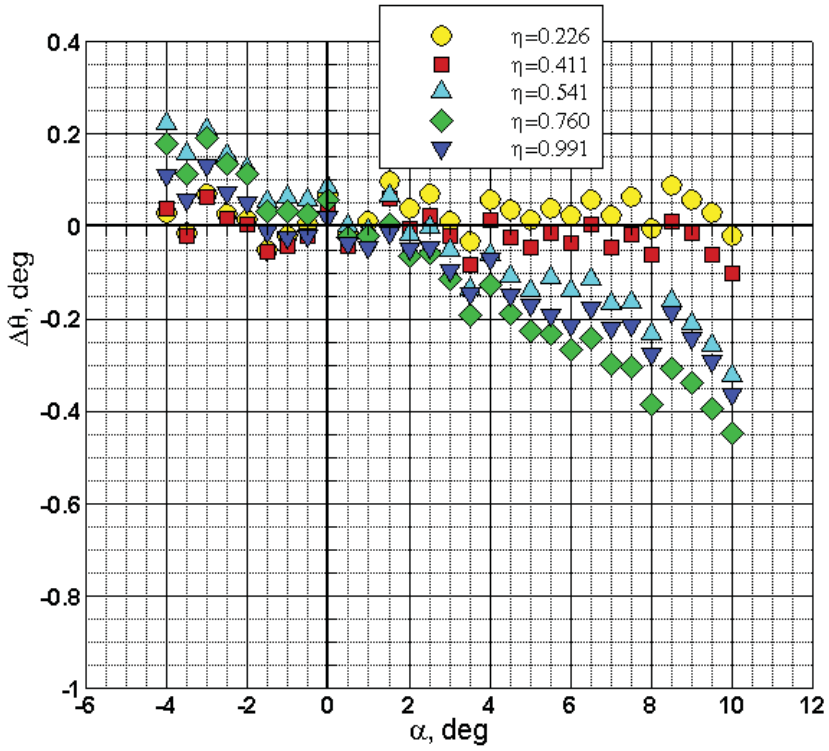

Figure 53. Differences between flapped wing and solid wing twist angles at all five measurement stations; $M_\infty = 2.7$, Re/ft = 4.0 x 10^6.

REPORT DOCUMENTATION PAGE

Form Approved
OMB No. 0704-0188

1. REPORT DATE *(DD-MM-YYYY)*	2. REPORT TYPE	3. DATES COVERED *(From - To)*
01- 04 - 2013	Technical Memorandum	

4. TITLE AND SUBTITLE

Experimental Investigation of Aeroelastic Deformation of Slender Wings at Supersonic Speeds Using a Video Model Deformation Measurement Technique

5a. CONTRACT NUMBER

5b. GRANT NUMBER

5c. PROGRAM ELEMENT NUMBER

6. AUTHOR(S)

Erickson, Gary E..

5d. PROJECT NUMBER

5e. TASK NUMBER

5f. WORK UNIT NUMBER

122711.03.07.07.16.80

7. PERFORMING ORGANIZATION NAME(S) AND ADDRESS(ES)

NASA Langley Research Center
Hampton, VA 23681-2199

8. PERFORMING ORGANIZATION REPORT NUMBER

L-20228

9. SPONSORING/MONITORING AGENCY NAME(S) AND ADDRESS(ES)

National Aeronautics and Space Administration
Washington, DC 20546-0001

10. SPONSOR/MONITOR'S ACRONYM(S)

NASA

11. SPONSOR/MONITOR'S REPORT NUMBER(S)

NASA/TM-2013-217977

12. DISTRIBUTION/AVAILABILITY STATEMENT

Unclassified - Unlimited
Subject Category 02
Availability: NASA CASI (443) 757-5802

13. SUPPLEMENTARY NOTES

14. ABSTRACT

A video-based photogrammetric model deformation system was established as a dedicated optical measurement technique at supersonic speeds in the NASA Langley Research Center Unitary Plan Wind Tunnel. This system was used to measure the wing twist due to aerodynamic loads of two supersonic commercial transport airplane models with identical outer mold lines but different aeroelastic properties. One model featured wings with deflectable leading- and trailing-edge flaps and internal channels to accommodate static pressure tube instrumentation. The wings of the second model were of single-piece construction without flaps or internal channels. The testing was performed at Mach numbers from 1.6 to 2.7, unit Reynolds numbers of 1.0 million to 5.0 million, and angles of attack from -4 degrees to +10 degrees. The video model deformation system quantified the wing aeroelastic response to changes in the Mach number, Reynolds number concurrent with dynamic pressure, and angle of attack and effectively captured the differences in the wing twist characteristics between the two test articles.

15. SUBJECT TERMS

Aerodynamics; Aeroelasticity; Angle of attack; Mach number; Model deformation; Optical measurement technique; Reynolds number; Supersonic speeds; Wind tunnel; Wing twist

16. SECURITY CLASSIFICATION OF:			17. LIMITATION OF ABSTRACT	18. NUMBER OF PAGES	19a. NAME OF RESPONSIBLE PERSON
a. REPORT	b. ABSTRACT	c. THIS PAGE			STI Help Desk (email: help@sti.nasa.gov)
					19b. TELEPHONE NUMBER *(Include area code)*
U	U	U	UU	57	(443) 757-5802